

## Learning quantum systems via out-of-time-order correlators

Thomas Schuster<sup>1,2,3,\*</sup> Murphy Niu<sup>1,4</sup> Jordan Cotler<sup>5</sup> Thomas O'Brien<sup>1</sup> Jarrod R. McClean<sup>1</sup> and Masoud Mohseni<sup>1,6,†</sup>

<sup>1</sup>Google Quantum AI, Venice, California 90291, USA

<sup>2</sup>Walter Burke Institute for Theoretical Physics and Institute for Quantum Information and Matter, California Institute of Technology, Pasadena, California 91125, USA

<sup>3</sup>Department of Physics, University of California, Berkeley, California 94720, USA

<sup>4</sup>Department of Computer Science, Joint Center for Quantum Information and Computer Science, University of Maryland, College Park, Maryland 20742, USA

<sup>5</sup>Society of Fellows and Black Hole Initiative, Harvard University, Cambridge, Massachusetts 02138, USA

<sup>6</sup>LSIP, Hewlett Packard Enterprise, Santa Barbara, California 93106, USA



(Received 17 August 2022; accepted 30 October 2023; published 22 December 2023)

Learning the properties of dynamical quantum systems underlies applications ranging from nuclear magnetic resonance spectroscopy to quantum device characterization. A central challenge in this pursuit is the learning of strongly interacting systems, where conventional observables decay quickly in time and space, limiting the information that can be learned from their measurement. In this work, we introduce a new class of observables into the context of quantum learning—the out-of-time-order correlator—which we show can substantially improve the learnability of strongly interacting systems by virtue of displaying informative physics at large times and distances. We identify two general scenarios in which out-of-time-order correlators provide a significant learning advantage: (i) when experimental access to the system is spatially restricted, for example, via a single “probe” degree of freedom, and (ii) when one desires to characterize weak interactions whose strength is much less than the typical interaction strength. We numerically characterize these advantages across a variety of learning problems, and find that they are robust to both read-out error and decoherence. Motivated by these physical scenarios, we introduce several learning tasks—including Clifford tomography, and learning the connectivity of an unknown unitary—in which out-of-time-order experiments have a provable exponential advantage over any learning protocol involving only time-ordered operations.

DOI: [10.1103/PhysRevResearch.5.043284](https://doi.org/10.1103/PhysRevResearch.5.043284)

### I. INTRODUCTION

Learning properties of quantum systems can pose challenges not present in their classical counterparts [1,2]. These differences often stem fundamentally from the existence of entanglement—measurements of a quantum system that is highly entangled with another system or the environment reveal little information from which to learn. In practical settings, these difficulties are most commonly encountered in *strongly interacting* quantum systems. Strong interactions can introduce nonlocal entanglement throughout the system at short time scales, and are found to thereby inhibit the learning of system properties (e.g., the Hamiltonian) from physical observables [3–7].

The ubiquity of strong interactions in experimental applications of quantum learning has spurred a variety of solutions

to this problem. For instance, in nuclear magnetic resonance (NMR) spectroscopy, a suite of technologies have been developed to controllably dampen undesired strong interactions between solid-state nuclear spins, which has enabled the identification of hitherto inaccessible molecular structures [8]. In a similar spirit, in quantum device characterization [9] and quantum sensing [6], dynamical decoupling control sequences [10] can effectively eliminate unwanted interactions and improve learning of the residual interactions.

Other approaches include learning by transducing quantum data from the system onto a quantum simulator [2–5], or learning from high-precision local measurements at early times, before entanglement has formed [11,12]. Nonetheless, owing to incomplete control or limited experimental precision, many physical systems remain unlearnable with existing approaches.

In this paper, we introduce a different paradigm for learning in strongly interacting quantum systems—learning via out-of-time-order correlators (OTOCs). First studied in early works on semi-classical methods [13] and NMR [14], the OTOC has more recently initiated a renaissance of work at the intersection of quantum information theory, many-body dynamics, and quantum gravity (e.g., Refs. [15–24]). Physically, OTOCs quantify the spread of local quantum information into highly nonlocal correlations [25]. Experimental

\*schuster@caltech.edu

†masoud.mohseni@hpe.com

Published by the American Physical Society under the terms of the [Creative Commons Attribution 4.0 International](https://creativecommons.org/licenses/by/4.0/) license. Further distribution of this work must maintain attribution to the author(s) and the published article's title, journal citation, and DOI.

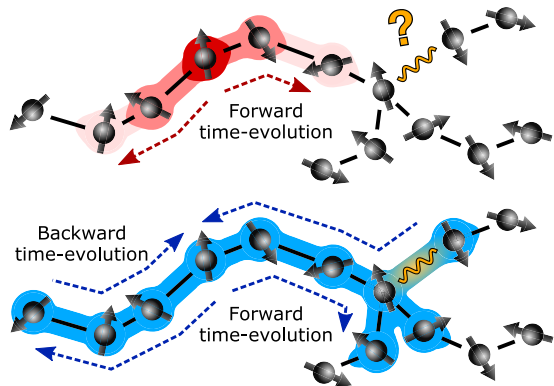


FIG. 1. Schematic of time-ordered correlators (TOCs) and out-of-time-order correlators (OTOCs) in strongly interacting systems. TOCs typically decay in  $O(1)$  times and distances (top, red), making it hard to learn features (yellow bond) that manifest only at late times. OTOCs utilize backwards time evolution to “refocus” many-body correlations (bottom, blue), enabling learning of such features.

measurements of the OTOC typically employ *reversed* time evolution to refocus these correlations, and have been performed on dozens of qubits in superconducting quantum processors and trapped ion quantum simulators, and hundreds of nuclear spins in NMR spectroscopy [26–30].

In this work, we utilize the OTOC as a *tool* for learning properties of strongly interacting quantum systems. Our application is motivated by a simple intuition: while time-ordered observables decay quickly as a system becomes entangled, out-of-time-order observables continue to fluctuate up to long times (Fig. 1). Guided by this intuition, we demonstrate the power of learning via OTOCs across a range of physical systems, supported by numerical studies, phenomenological estimates, and rigorous information-theoretic proofs. We begin in locally interacting systems, where we identify two general scenarios in which OTOCs provide a strong learning advantage: (i) when experimental access to the system is spatially restricted, for example, via a single “probe” qubit [31–33], and (ii) for detecting weak interactions in an otherwise strongly interacting system [6,9]. We characterize these advantages using both information-theoretic measures (the Fisher information) and performance metrics for concrete learning tasks. Moreover, we find that the advantages are robust to experimental read-out error and time-reversal imperfections arising from strong coupling with an environment or decoherence.

Finally, motivated by recent advances in *provable* learning advantages [4,5,34], we introduce two learning tasks that involve characterizing properties of unitary operations if given oracle access. Our first task concerns learning the connectivity of a unitary operation. We show that a single out-of-time-order experiment can learn the connectivity, while in a companion work [35] we establish the exponential difficulty of this task for any time-ordered learning protocol. Our second task shows that learning via OTOCs can be particularly advantageous in restricted computational models. We consider performing tomography of a Clifford unitary. We prove that out-of-time-order experiments provide an exponential advantage over

time-ordered experiments for this task in the presence of any nonzero read-out error, or when read-out is restricted to a single qubit (related to the DQC1 model of quantum computation [36,37]).

## II. BEHAVIOR OF TIME-ORDERED VERSUS OUT-OF-TIME-ORDER CORRELATORS

We begin by reviewing the phenomenology of time-ordered and out-of-time-order correlators in ergodic locally interacting systems (Fig. 1). A time-ordered correlator (TOC) is defined as any correlation function that takes the following general form:

$$C_{\text{TOC}} = \text{tr}(A_k(t_k) \dots A_1(t_1) \rho B_1(t'_1) \dots B_\ell(t'_\ell)), \quad (1)$$

where the operators  $A, B$  increase in time away from the initial density matrix  $\rho$ , i.e.,  $t_k > \dots > t_1$  and  $t'_\ell > \dots > t'_1$ . Time-ordered correlators can be measured by evolving the state  $\rho$  forward in time (e.g., via Hamiltonian evolution  $O(t) = e^{iHt} O e^{-iHt}$ ) while applying intermediary quantum operations at each time  $t_i, t'_j$  [38]. Any correlation function that does not obey this form is called an *out-of-time-order* correlator.

A common example of a time-ordered correlator is the two-point function,

$$C_{\text{TOC}} = \langle V_x(t) W_{x'}(0) \rangle, \quad (2)$$

where  $V_x, W_{x'}$  are local operators at sites  $x, x'$ . Here,  $\langle \cdot \rangle \equiv \text{tr}(\cdot)/2^L$  denotes the infinite temperature trace for  $L$  qubits. We can also consider the correlator in a specific initial state,  $C_{\text{TOC}}^\psi = \langle \psi | V_x(t) W_{x'}(0) | \psi \rangle$ . Such correlators measure the spread of local quantities in space and time; for instance, how much spin prepared at site  $x'$  at time zero has transferred to site  $x$  at time  $t$ . A wide range of literature on thermalization in strongly interacting systems has found that local TOCs typically decay quickly, i.e., in  $O(1)$  times, to their thermal values [39]. This quick decay can inhibit learning tasks, since no additional information can be acquired from the TOC at times after the decay has occurred [7].

Meanwhile, the prototypical out-of-time-order correlator is the four-point function [25],

$$C_{\text{OTOC}} = \langle V_x(t) W_{x'}(0) V_x^\dagger(t) W_{x'}(0) \rangle, \quad (3)$$

with local unitary operators  $V_x, W_{x'}$ . Again, we can also define the OTOC for a specific initial state via  $C_{\text{OTOC}}^\psi = \langle \psi | V_x(t) W_{x'}(0) V_x^\dagger(t) W_{x'}(0) | \psi \rangle$ . Unlike time-ordered correlators, OTOCs typically require both forwards *and* backwards time evolution to measure [25,35]. (Importantly for our application, nearly all experimental techniques for time-reversal rely only on the type of interaction being reversed and require no knowledge of the specific Hamiltonian, which one might wish to learn. For example, the same pulse sequence reverses a spin Hamiltonian with dipolar couplings regardless of the specific coupling strengths [29].) Physically, the OTOC probes whether information encoded at site  $x'$  at time zero is contained in correlations involving site  $x$  at time  $t$ . This is quantified by the squared commutator of a time-evolved operator at  $x$  with a local operator at  $x'$ ,  $\langle [V_x(t), W_{x'}(0)]^2 \rangle = 1 - C_{\text{OTOC}}$ . In local strongly interacting systems, operators are expected to spread ballistically according to the connectivity

of the system [23,40,41]. Crucially, this spread continues for a duration proportional to the system's spatial extent  $\sim L$  by which time the information has been delocalized across the entire system.

This phenomenology leads to two central intuitions for learning from OTOCs. First, the dynamics of the OTOC contain information primarily about the connectivity of the system under study. Second, the OTOC continues to reveal such information up to  $O(L)$  times, long after TOCs have decayed. Notice that this timescale increases as the system size increases. In what follows, we apply these intuitions to identify two broad regimes where access to OTOCs provides a significant learning advantage.

### III. QUANTUM LEARNING SCENARIOS

The learning tasks we consider all involve estimating properties of an unknown Hamiltonian from experiments involving time evolution under the Hamiltonian. For concreteness, we assume that the experiments consist of measuring correlation functions of the form of Eqs. (3) and (2). We will compare the performance of learning algorithms for different tasks when the algorithm has access to out-of-time-order correlation functions [Eq. (3)] versus time-ordered correlation functions [Eq. (2)]. From the physical arguments in the preceding section, we anticipate that access to more general experimental measurement schemes within a given time-ordering, e.g., via shadow tomography or related techniques [42–44], will not qualitatively change the observed physics (see Appendix A for additional discussion).

Our learning tasks fall roughly into two categories. First, we consider classification-based tasks, where one's goal is to classify some discrete high-level feature of the Hamiltonian such as the connectivity of its interactions. Second, we consider parameter-learning tasks, where one's goal is to learn the value of a continuous parameter of the Hamiltonian to the highest precision possible. We will see in the subsequent sections that access to OTOCs provides significant advantages for both sets of tasks, demonstrating the generality of our approach.

In both cases, solving the learning tasks requires comparing the experimental data from the unknown Hamiltonian to data generated by a trusted classical or quantum simulation. If the dynamics can be analytically solved or estimated, the data from the trusted simulator could also be replaced with an analytic solution. Such a comparison is necessary in order to relate features of the Hamiltonian to the experimental measurement outcomes. For example, if one is estimating a parameter  $J$  from a measured correlation function  $C$ , a simple approach would be to simulate the correlation functions  $C(J)$  for various values of  $J$  and see which value matches the experimental result. We emphasize that our use of device (2) does not rely on knowledge of the parameters of the Hamiltonian (1).

In the classification tasks, the goal is to predict some discrete property of the unknown Hamiltonian from measurements of its correlation functions. We suppose that the Hamiltonian is unknown but is drawn from some known distribution (e.g., each of the terms in the Hamiltonian takes a random value within a known range), which reflects the

prior knowledge of the experimenter. Since these tasks involve high-dimensional input data (e.g., the correlation functions for many different sites  $x$  and times  $t$ ), we approach them using machine learning techniques. Specifically, we envision using a trusted simulator to compute the correlation functions for ensembles of Hamiltonians with different values of the discrete property. These ensembles can then be used to train a classical machine learning model that predicts the desired property from the correlation functions. Once the model is trained, we can apply the model to the experimentally measured correlation functions to predict the desired property of the unknown Hamiltonian. We emphasize that this use of the trusted classical or quantum simulator does not rely on knowledge of the parameters of the unknown Hamiltonian. We describe further details of the machine learning procedure in the following sections, within the context of the specific learning scenarios.

In the parameter-learning tasks, instead of solving the task explicitly, we quantify the *optimal* learnability of the parameter using the Fisher information (FI). The FI quantifies the amount of information that a random variable (e.g., a correlation function  $C$ , measured within some read-out error  $\delta$ ) carries about an unknown parameter (e.g., a Hamiltonian parameter,  $J$ ). If one assumes that read-out errors are normally distributed, the FI is simply a squared derivative,  $\text{FI}(J|C) \equiv \delta^2 \text{FI}(J|C; \delta) = |\partial C / \partial J|^2$ , where we remove the  $\delta$ -dependence by introducing a factor  $\delta^2$ . The FI bounds the learnability of the parameter for any learning strategy based on the given correlation function. Specifically, the Cramer-Rao bound of statistics states that the variance in any estimate of the parameter is lower bounded by the inverse Fisher information [45]. If the read-out errors are normally distributed, the Cramer-Rao bound is easily achieved using the sample mean, i.e., calculating the average correlator  $C_{\text{avg}}$  over measurement outcomes, and setting  $J$  such that  $C(J) = C_{\text{avg}}$ .

This logic extends straightforwardly to the case when the experimenter has access to many correlation functions. In this scenario, if the read-out error is shot-noise limited, the optimal learning strategy would be to identify the single correlator with the highest FI and perform many repeated measurements of this correlator. The repeated measurements minimize the shot-noise  $\delta$ . This in turn minimizes the variance in the parameter estimate. In the numerical examples that follow, we thus quantify the learnability of a parameter  $J$  by taking the maximum of the FI over all available correlation functions,  $\max_C \text{FI}(J|C)$  [46].

### IV. LEARNING WITH RESTRICTED ACCESS

The first regime we consider is learning in systems with *restricted access*. Specifically, motivated by recent advances in solid-state defects [32,33,47,48] and NMR [49–51], we focus on the scenario where an experimenter has state preparation and read-out capabilities over only a single “probe” qubit interacting with a larger system that one wishes to learn. We note that high-fidelity OTOC measurements have already been achieved in similar setups by using rapid global pulse sequences to reverse time evolution [29,52,53]. Previous theoretical approaches to learning in this scenario have been

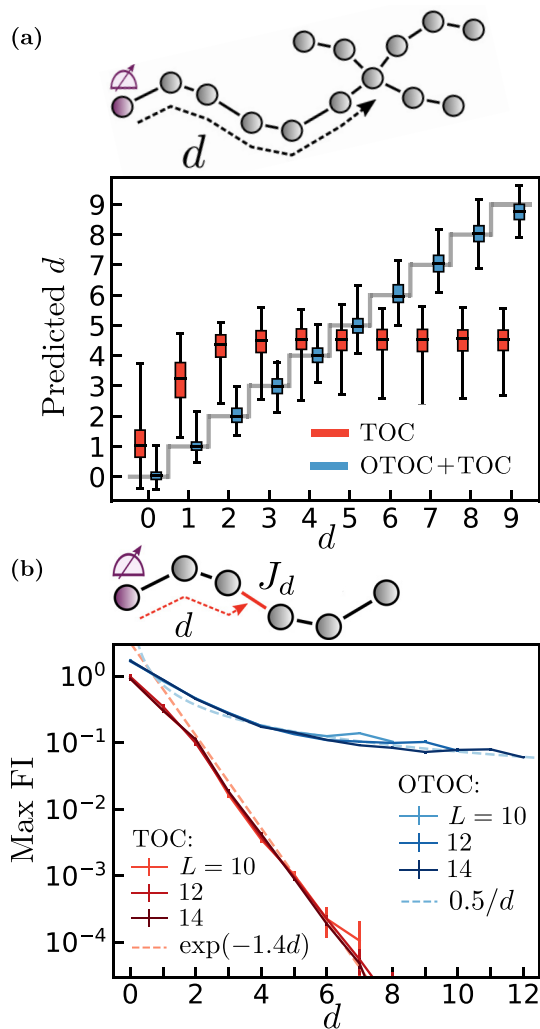


FIG. 2. Learning with state preparation and read-out restricted to a probe qubit, and local unitary control over the remaining system. (a) Results from SVM regression for learning the distance,  $d$ , in the spin geometry shown, with access to TOCs (red) or both TOCs and OTOCs (blue). Color bars (black ticks) denote 75% (100%) percentiles of predictions on 200 disorder realizations, and grey step function represents the actual  $d$ . (b) Fisher information,  $FI(J_d|C)$ , of an interaction,  $J_d$  (top; red line), a distance  $d$  away from the probe (top; purple circle), maximized over all correlators,  $C$ , in an  $L$ -qubit 1D chain. The FI decays exponentially in  $d$  when  $C$  is time-ordered (red), and algebraically,  $\sim 1/d$ , when  $C$  is out-of-time order (blue).

limited to noninteracting dynamics [31,51,54–57]. Meanwhile, experiments have found that it is in general difficult to learn features of a system that are distant from the probe qubit [32,33]. In strongly interacting systems, this difficulty can be understood from the quick decay of correlation functions in space and time. Here, we provide evidence via phenomenological estimates (Appendix B) and numerical simulations (Fig. 2) that access to OTOCs can exponentially improve the learnability of distant features.

To be concrete, we will consider two scenarios for the degree of experimental control over the larger system: local unitary control and global unitary control. The latter, weaker

form of control is more common in current experiments [32,48–50], but the former is also achievable depending on, for example, the strength and localization of optical addressing of the larger system [58]. We will also assume that the larger system begins in an infinite temperature (i.e., maximally mixed) state, which is the natural scenario in NMR and solid-state defect setups [47,49]. A simple class of measurement protocols proceeds as follows.

- (1) Prepare the probe qubit  $p$  in an eigenstate of an operator  $V_p$ , such that the density matrix of the entire system is  $\rho = \frac{1}{2}(\mathbb{1}_p + V_p) \otimes \frac{1}{2^{L-1}} \mathbb{1}_{\text{sys}}$ .
- (2) Time-evolve by time  $\tau$ .
- (3) Perturb the system by a unitary operation  $W$ . Depending on the degree of experimental control, this might be a global spin rotation or a local operation on a qubit  $x$ .
- (4) Time-evolve by a time  $\tau'$ .
- (5) Read out the expectation value of  $V_p$  on the probe qubit.

Taking  $\tau, \tau'$  to be positive (e.g.,  $\tau = \tau' = t/2$ ), this allows measurement of time-ordered correlation functions of the form  $\langle V_p(t) W(t/2) V_p(0) W^\dagger(t/2) \rangle$ . With access to reversible time evolution (e.g.,  $\tau = -\tau' = t$ ), the above protocol also allows measurement of out-of-time-order correlation functions  $\langle V_p(0) W(t) V_p(0) W^\dagger(t) \rangle$ . We note that, in step 1, the probe qubit does not need to be in an exact eigenstate and could instead be initialized with any finite polarization  $f$  of the  $V_p$  operator, i.e., replacing  $\mathbb{1}_p + V_p \rightarrow \mathbb{1}_p + fV_p$ .

We begin our exploration of learning via OTOCs by introducing a concrete learning task. We begin with the case of local unitary control. We consider the following scenario: one is given access to a quantum system consisting of two spin chains intersecting at a distance  $d$  from a probe qubit [Fig. 2(b)]. The value of  $d$  as well as the specific Hamiltonian parameters of the system are unknown (see below for the specific distribution that the Hamiltonian is drawn from). The goal is to learn the value of  $d$ , i.e., the geometry of the system, from measurements of the system's correlation functions. This task is a toy model meant to explore the ability of the OTOC to learn distant geometric features of a system in restricted access scenarios. As discussed in the previous section, we approach this task by training a classical machine learning model to predict  $d$  from the measured correlation functions, using training data generated by either a classical computer or a separate trusted quantum simulator.

Let us briefly summarize our numerical simulations in more detail (see Appendix A for a complete description). Throughout this work, we consider spin systems with disordered on-site fields,  $H_f = \sum_{i,\alpha} h_i^\alpha \sigma_i^\alpha$  with  $h_i^\alpha \in [-1, 1]$  and  $\alpha = x, y, z$ , and disordered dipolar interactions between neighboring spins,  $H_c = \sum_{\langle ij \rangle} J_{ij} (\sigma_i^x \sigma_j^x + \sigma_i^y \sigma_j^y - 2\sigma_i^z \sigma_j^z)$  with  $J_{ij} \in [0.6, 1.4]$ . We specify to Floquet dynamics consisting of alternating applications of  $H_f$  and  $H_c$  for time  $T = \pi/2$ , and simulate time evolution via Krylov-subspace methods [59]. We expect that learning Floquet dynamics will be qualitatively similar to learning time-independent Hamiltonian dynamics at moderate times and distances, which we are restricted to in our numerics (see Appendix C for numerical support of this statement). At larger distances, we expect Hamiltonian dynamics to be dominated by hydrodynamics of the conserved energy (Appendix B) and the two will differ. We

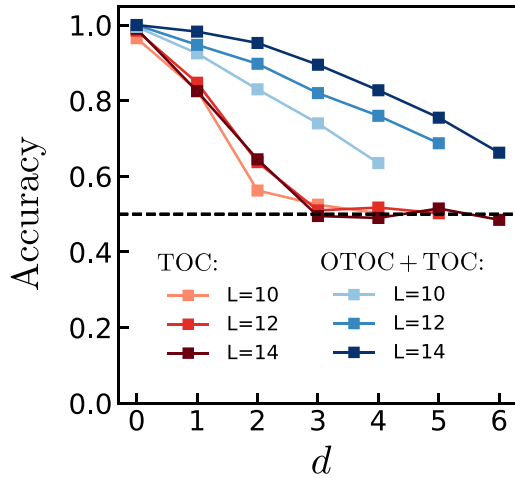


FIG. 3. Learning in the restricted access scenario with global unitary control for TOCs (red) and both OTOCs and TOCs (blue). Results are for a binary classification task to characterize whether the system geometry is a line or loop. For probes at distances  $d \gtrsim 3$  from the boundary, learning via TOCs gives trivial accuracy. Meanwhile, learning via OTOCs gives an accuracy that increases with the system size  $L$ .

verify that the dynamics studied are in the ergodic regime, and not many-body localized, by observing the decay of two-point autocorrelation functions in Appendix A.

Returning to the learning task at hand, we train a support vector machine (SVM) on 3000 randomly drawn Hamiltonians (300 for each value of  $d = 0, \dots, 9$ ), and test its performance on 2000 additional Hamiltonians. The input to the machine learning model consists of the correlations functions described above for a range of times  $t$  and local operators  $W_x$ . To mimic the conditions of realistic experimental settings, we add a Gaussian distributed “read-out error” to all correlation functions, with mean zero and standard deviation  $\delta = 3\%$ . The model’s predictions as a function of the actual value of  $d$  are displayed in Fig. 2(b), for learning either via TOCs (red) or both TOCs and OTOCs (blue). We find that learning via OTOCs allows accurate predictions of  $d$  within  $\pm 1$  of its actual value for all distances probed (up to  $d = 9$ ). In contrast, with access to only TOCs, the model performs significantly worse for all  $d$  and resorts to nearly random guessing for  $d \gtrsim 3$ .

We now turn to the case of global unitary control. We consider a slightly simpler learning task to reflect the lesser information available with global control. Namely, we suppose that one is given access to an unknown quantum spin chain with either a line or loop geometry (i.e., either open or periodic boundary conditions). In the line geometry, we suppose the probe qubit is a distance  $d$  from the boundary. The goal is to use the correlation functions of the system, involving global spin rotations  $W = e^{i\phi \sum_j \sigma_j^\alpha}$  for various  $\phi, \alpha$ , to perform binary classification of the two possible geometries. Using the same machine learning procedure as in the previous task, we indeed find a sizable learning advantage for OTOCs (Fig. 3). This advantage is particularly pronounced for distances  $d$  greater than only a few qubits, since after this the TOC provides little information. Moreover, we observe that

this advantage *increases* with increasing system size. Indeed, in the limit of large system sizes in ergodic dynamics, the learning task we consider is strictly solvable with OTOCs and strictly impossible with TOCs. We expect that learning tasks involving more complicated geometric features might be solvable in larger-size systems with global unitary control as well. In Appendix C, we discuss an additional threefold classification task, and how learning is modified when the experimentalist has only global state preparation and read-out.

To quantify the learning advantage of OTOCs for more precise learning tasks, we turn to the Fisher information (FI). We numerically compute the FI in ergodic 1D spin chains, where one seeks to learn a coupling  $J_d$  lying a distance  $d$  away from a probe qubit [Fig. 2(b) inset] [31,51,54–57]. We consider the same set of correlation functions as specified for the learning task in Fig. 2(a). In Fig. 2(b), we plot the maximum Fisher information  $\max_C \text{FI}(J|C)$  over all correlation functions (i.e., over all  $x, t$ ), averaged over 200 and 1000 disorder realizations for TOCs and OTOCs respectively. We find that the maximum FI of TOCs (red) decays exponentially in the distance  $d$  from the probe qubit. In contrast, the maximum FI of OTOCs (blue) follows a slow algebraic decay,  $\sim 1/d$ , thereby achieving a multiple-order-of-magnitude advantage over TOCs even at modest distances,  $d \gtrsim 3$ . This algebraic decay arises from the  $\sim \sqrt{t}$  broadening of the OTOC wavefront in time [23], see Appendix B for a full phenomenological derivation. In Appendix B, we also provide phenomenological estimates for the Fisher information when the experimentalist has only global unitary control over the larger system.

## V. LEARNING WEAK INTERACTIONS

We now turn to our second learning scenario: characterizing weak interactions in an otherwise strongly interacting system. Such characterization is notoriously difficult because weak interactions take long times to manifest (of order the inverse interaction strength), at which point TOCs have decayed due to the strong interactions. Previous approaches require either dynamical decoupling of the strong interactions [6,9] or high-precision measurements at early times [11,12]. We will now show that access to OTOCs allows one to side-step these requirements when characterizing weak interactions that *change the connectivity* of a strongly interacting system. Notably, in contrast to the previous learning scenario, this advantage holds even when the experimenter is capable of measuring all local correlation functions of the system of interest.

For concreteness, we specialize to 1D spin chains with a single “weak link” interaction, of strength  $J_\ell$  much less than the typical interaction strength  $J$  [see Fig. 4(b) inset]. We consider TOCs and OTOCs of the form Eqs. (2) and (3), where  $x, x'$  run over all qubits in the system.

We begin as before with a concrete learning task. Specifically, we suppose that one is given access to a spin chain with unknown Hamiltonian parameters and either no link interaction ( $J_\ell \rightarrow 0$ ) or a fixed nonzero weak link interaction strength  $J_\ell$ . For each fixed value of  $J_\ell$ , we train a binary SVM classifier on the correlation functions [Eqs. (2) and (3)] of 300 disorder samples, again including a read-out error  $\delta = 3\%$  in each correlator value. We test model performance on 200

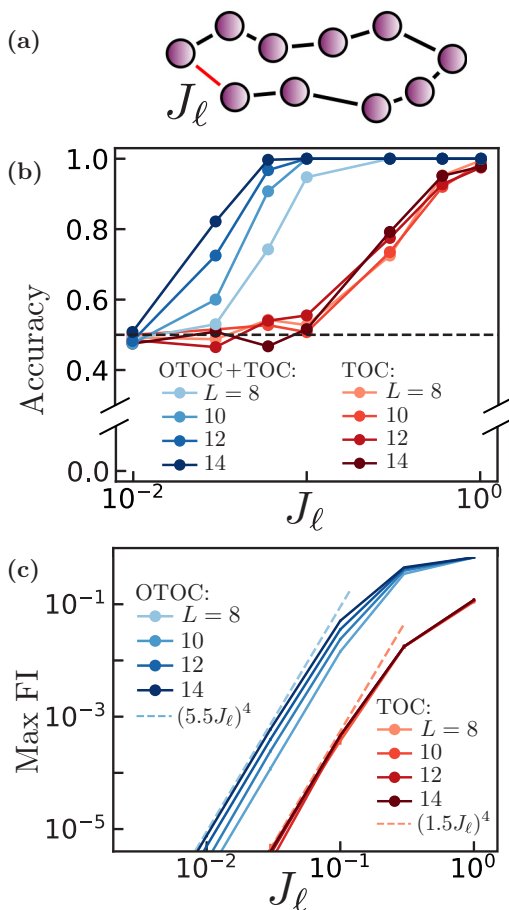


FIG. 4. (a) Learning a weak “link” interaction (red line) in a 1D spin chain with otherwise strong interactions (black lines). (b) Accuracy of binary SVM classification of whether the link is present or absent, as a function of the link strength  $J_\ell$  and at fixed read-out error  $\delta = 3\%$ . Learning via OTOCs can detect smaller  $J_\ell$  as  $L$  increases, while the TOC can only detect relatively large  $J_\ell$ , independent of  $L$ . (c) The maximum Fisher information  $\text{FI}(\ln(J_\ell)|C)$  of  $J_\ell$  decays  $\sim J_\ell^4$  for small  $J_\ell$ , and is enhanced in OTOCs (blue) compared to TOCs (red) by a factor that increases with  $L$ .

additional samples; the resulting classification accuracies are shown in Fig. 4(b). We observe the following general trends: (i) the accuracy decreases as  $J_\ell$  decreases; (ii) learning via both OTOCs and TOCs (blue) allows detection of  $\sim 10$  times smaller  $J_\ell$  than learning via only TOCs (red); and (iii) OTOCs allow detection of increasingly small  $J_\ell$  as the size  $L$  of the chain increases.

We can also use this learning task to explore how the learning advantage of OTOCs depends on the choice of initial state. Indeed, in many quantum simulation platforms where detecting weak interactions is of interest, the most natural choice of initial state is a simple product state. In Fig. 5, we show the accuracy of classification for the same learning task as above, but replacing the infinite-temperature correlators with their values in several specific initial product states (see Appendix A for details). For all states considered, the results qualitatively resemble the infinite-temperature setting. Compared to the infinite-temperature setting, learning from TOCs displays a modest improvement for some initial states at

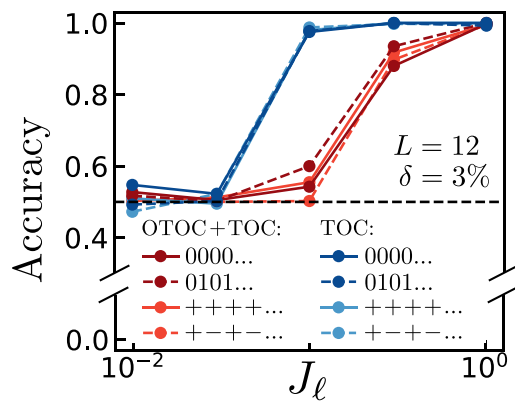


FIG. 5. Learning a weak link interaction with initial product states. Accuracy of binary classification of whether the link is present or absent for four different initial product states,  $\{|0\rangle^{\otimes L}, |01\rangle^{\otimes L/2}, |+\rangle^{\otimes L}, |+-\rangle^{\otimes L/2}\}$ , with fixed read-out error  $\delta = 3\%$  and system size  $L = 12$ . Learning via OTOCs provides a persistent advantage compared to learning via TOCs for all product states considered, and qualitatively resembles the results for infinite-temperature correlators in Fig. 4(b).

moderate coupling strengths,  $J_\ell \sim 0.3$ , although the steep decrease in accuracy for smaller values of the couplings remains. Meanwhile, the accuracy of learning via OTOCs displays remarkably little variation for different initial states. These results conform to our expectation for ergodic dynamics, in which we expect a system to quickly lose memory of its initial state. Since learning via OTOCs relies predominantly on the values of correlators at later times, it displays a weaker dependence on the initial state.

To understand this behavior analytically, we first note that the optimal correlation functions for detecting the link will typically involve operators lying immediately adjacent to that link, on both of its sides. These correlators measure either the transfer of spin polarization (for TOCs) or operator support (for OTOCs) across the link, and will be nontrivial only if the link interaction strength is nonzero. For TOCs, one expects spin polarization to cross the link incoherently, at a rate  $\sim J_\ell^2/J$ , where  $J$  is the typical strong interaction strength. Combined with an overall exponential decay of spin in time (if the system has no conserved quantities), we expect  $C_{\text{TOC}} \sim (J_\ell^2/J)t e^{-Jt}$ . For OTOCs, one expects an operator’s support to cross the link at a similar rate,  $1 - C_{\text{OTOC}} \sim (J_\ell^2/J)t$ . Crucially however, this growth persists until much *later* times,  $t \sim L/J$ , at which information traveling “around” the chain will abruptly cause the OTOC to decay to zero. The optimal time for detecting the link occurs when these correlators are maximized, since each is zero in the absence of the link. The TOC is maximized at an order one time  $t \sim 1/J$ , at which the correlator magnitude  $C_{\text{TOC}} \sim J_\ell^2/J^2$  is suppressed by the square of the weak link interaction strength. In contrast, the OTOC is maximized at a much later time  $t \sim L/J$ , and thereby features a magnitude  $1 - C_{\text{OTOC}} \sim L(J_\ell^2/J^2)$ . In both cases we see that detection of the link becomes more difficult as the link strength decreases. Detection via the OTOC is enhanced by a factor of  $L$ , which captures the connectivity change associated with the link.

We confirm these estimates quantitatively by computing the Fisher information of the link interaction strength. In Fig. 4(b), we plot the maximum Fisher information  $\max_C \text{FI}(\ln(J_\ell)|C)$  over all local correlation functions, averaged over 100 disorder realizations. Here, we consider the logarithm of the link interaction strength in order to appropriately compare the Fisher information over multiple orders of magnitude of the interaction. The Fisher information of  $\ln(J_\ell)$  bounds the learnability of the interaction strength as a *percentage* of its actual value. Applying our phenomenological estimates, we predict that  $\text{FI} \sim J_\ell^4/J^4$  for TOCs, and  $\text{FI} \sim L^2 J_\ell^4/J^4$  for OTOCs. Observing Fig. 4(b), we indeed find that the FI is suppressed by  $\sim J_\ell^4$  (dashed lines) for small  $J_\ell$ , and displays a multiplicative advantage for OTOCs (blue) compared to TOCs (red), which grows as  $L$  increases.

### VI. EFFECT OF EXPERIMENTAL ERRORS

Let us now address the impact of experimental errors on learning. We begin with errors that accumulate throughout time evolution. These may occur from extrinsic decoherence or imperfect time-reversal dynamics, each of which disrupt the nonlocal correlations probed by the OTOC [27,29,30,60–62]. While this disruption can be mitigated via independent error estimates [27,60], for sufficiently large errors these estimates involve measuring quantities of small magnitude (comparable to the TOC), squandering the OTOC’s learning advantage. In Appendix B, we estimate that our previous results are modified in the presence of a small local error rate  $\varepsilon \ll J$  as follows: in the first learning regime, the OTOC maintains its advantage up to distances  $d \lesssim J/\varepsilon$ ; in the second regime, the  $L$ -fold advantage is replaced by a  $(\min\{L, \sqrt{J/\varepsilon}\})$ -fold advantage.

In practice, we find that learning via OTOCs remains robust even to relatively large amounts of imperfect time-reversal [Fig. 6(a)]. We study this numerically in the “weak interaction” learning problem of Fig. 4(b). As a concrete instance of imperfect time-reversal, we take the spins to be coupled to an extrinsic cavity mode and assume that the spin dynamics are perfectly reversed but the cavity dynamics and spin-cavity coupling  $g$  are unreversed. We find that access to OTOCs substantially improves the classification accuracy even for quite large spin-cavity couplings  $g \sim 0.5$ , up to half the spin-spin interaction strength.

We can also examine the dependence of learning on read-out errors, namely where one measures a correlator  $C$  up to additive error. Indeed, we have already incorporated a realistic read-out error  $\delta = 3\%$  in our previous numerical studies [Figs. 2(a), 4(a), and 6(a)]. Intuitively, we expect larger read-out errors to make learning more difficult; however, we have little reason to expect read-out error to change the *relative* advantage of OTOCs compared to TOCs. We test this numerically by repeating the analysis of Fig. 4(b) for various read-out errors,  $\delta$ . For each  $\delta$ , we compute the minimum link strength  $J_\ell^*$  that can be learned with  $>90\%$  accuracy [Fig. 6(b)]. For errors  $\delta \gtrsim 10^{-3}$ , our results agree well with analytic estimates, which predict  $(J_\ell^*/J)^2 \sim \delta$  for TOCs and  $(J_\ell^*/J)^2 \sim \delta/L$  for OTOCs. Intriguingly, for sufficiently small errors  $\delta \lesssim 10^{-3}$ , the minimum link strength detectable with TOCs *saturates* to a finite value  $J_\ell^* \sim 0.2$ . Below this value, sample-to-sample

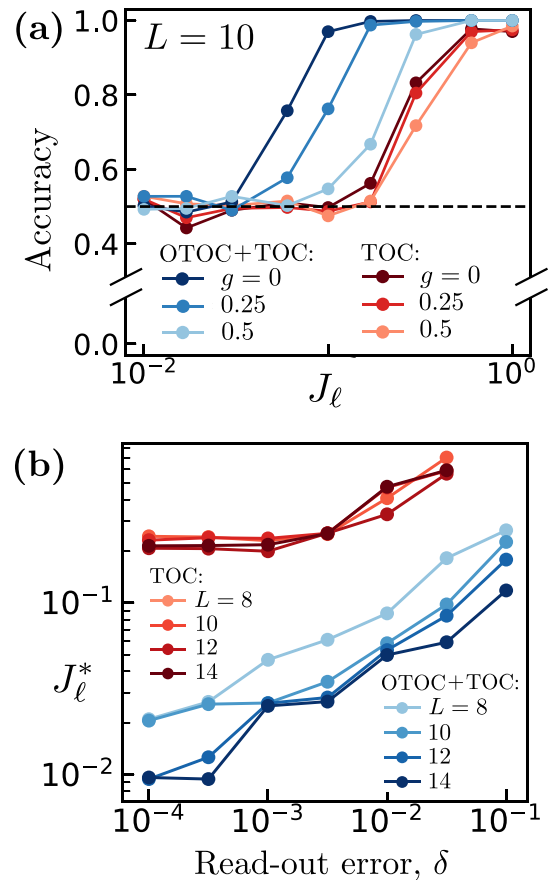


FIG. 6. Learning as a function of experimental error, in the “weak interaction” learning task of Fig. 4(a). (a) Accuracy of binary SVM classification as in Fig. 4(a), now with a coupling  $g$ , to an extrinsic cavity mode that is not time-reversed (cavity frequency  $\omega = 1.7$ ). Despite imperfect time-reversal, learning via OTOCs continues to provide an advantage up to large spin-cavity couplings  $g \sim 0.5$ . (b) The minimum link strength  $J_\ell^*$  classifiable with  $>90\%$  accuracy as a function of read-out error  $\delta$ , obtained by repeating Fig. 4(a) for each  $\delta$ . The minimum link strength in general decreases with decreasing  $\delta$ ; for learning via TOCs, this decrease plateaus for  $\delta \lesssim 0.1\%$ , indicating that learning below this value is not limited by read-out error.

fluctuations of the TOC cause the learning task to be difficult regardless of the read-out error.

### VII. PROVABLE ADVANTAGE FOR CLASSIFYING UNITARY CONNECTIVITY

We have so far demonstrated the learning power of OTOCs using phenomenological arguments and numerical simulations, owing to the difficulty of obtaining analytic results for ergodic Hamiltonian systems. Complementary to these results, in this and the following section, we introduce two learning tasks in which the OTOC provides a provable exponential advantage over time-ordered measurement strategies.

In this section, we consider the following binary classification task.

*Disjoint unitary problem.* One is given oracle access to either (i) a fixed,  $n$ -qubit Haar-random unitary  $U$ , or (ii) a

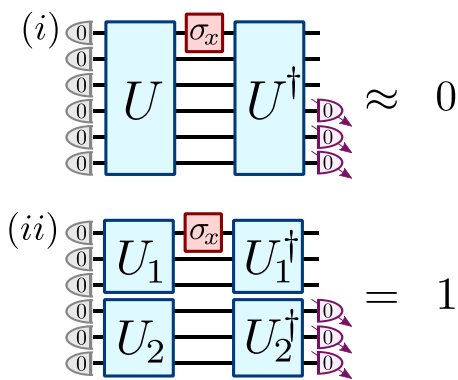


FIG. 7. Solution to the disjoint unitary problem with out-of-time-order measurements. The state  $|0\rangle^{\otimes n}$  is prepared and the unknown unitary (either  $U$  or  $U_1 \otimes U_2$ ) is applied. Next  $\sigma_x$  is applied to the first qubit, followed by the inverse of the unknown unitary. Finally, it is checked if the second block of  $n/2$  qubits ends up in the all zero state. If so, then the hidden unknown unitary is  $U_1 \otimes U_2$  as per case (ii); if not, then the unknown unitary is  $U$  as per case (i).

tensor product of two fixed,  $n/2$ -qubit Haar-random unitaries,  $U_1 \otimes U_2$ . The task is to determine which of (i) or (ii) is realized.

Qualitatively, this problem resembles the Hamiltonian learning scenarios identified previously. First, the feature we seek to learn—the connectivity of the unitary—directly determines how information spreads through the system, as measured by the OTOC. Second, a Haar-random unitary is inherently “strongly interacting,” which causes time-ordered measurements to decay and thus provide little information.

In Fig. 7, we show that the disjoint unitary problem can be solved with a constant number (with respect to  $n$ ) of queries to the oracle and its time-reverse  $U^\dagger$ , by measuring an out-of-time-order observable. Letting  $V$  denote the unknown unitary (either  $U$  or  $U_1 \otimes U_2$ ), the OTOC is

$$\text{OTOC}(V) = \text{tr}(\mathbb{1}_{\frac{n}{2}} \otimes |0\rangle\langle 0|^{\otimes \frac{n}{2}} \{V^\dagger \sigma_x^1 V |0\rangle\langle 0|^{\otimes n} V^\dagger \sigma_x^1 V\}).$$

In case (i), the OTOC is near zero with probability exponentially close to one [35]. In case (ii), the OTOC is one, since the two subsystems are not coupled by  $U_1 \otimes U_2$ . Thus, with probability exponentially close to one, the two cases may be distinguished with a single query to the unknown unitary and its time-reverse. In contrast, in a companion work [35], we prove that any time-ordered learning protocol requires an exponential number  $\Omega(2^{n/4})$  of queries of the unknown unitary to solve the disjoint unitary problem. Our proof applies even to adaptive measurement strategies, and leverages novel contemporary techniques from quantum learning theory [4,5,34].

### VIII. PROVABLE ADVANTAGE FOR LEARNING WITH IMPERFECT READ-OUT

As we saw in Sec. IV, out-of-time-order experiments can provide a particularly substantial learning advantage in systems with imperfect read-out capabilities. We now establish this advantage rigorously. We consider two experimental scenarios: first, where read-out is restricted to a single qubit,

and second, where full read-out is allowed, but occurs with a nonzero error  $\delta$  per qubit.

The first scenario is motivated by the advantages we observed for learning in spin chains with restricted access in Sec. IV. This setting has been the subject of significant previous study in the quantum computing community, and is known as the deterministic quantum computation with one clean qubit (DQC1) model of quantum computation [36,37]. Experiments within this model are restricted to act on an initial state  $\rho = |0\rangle\langle 0| \otimes (\mathbb{1}/2)^{\otimes(n-1)}$ , which is maximally mixed on all but the first qubit. Measurements are similarly restricted to act on only the first qubit. Nevertheless, arbitrary unitary operations are allowed in between state preparation and measurement. We note, in advance, that our hardness results for Clifford tomography in the DQC1 model will in fact hold when either the initial state or the final read-out is restricted (see Appendix D), we do not require both.

Our second scenario is, in some ways, an extension of the first. Indeed, we can view the nonmeasured qubits in the DQC1 model as being fully “decohered” at the conclusion of the experiment. If we consider instead a finite local read-out error  $\delta$  on each qubit, this will decohere nonlocal correlations in the final quantum state that involve more than  $O(1/\delta)$  qubits. If a learning algorithm relies on these nonlocal correlations, then a nonzero read-out error may substantially increase the difficulty of the learning task. This opens the door to a learning advantage for out-of-time-order experiments, since backwards time evolution can refocus nonlocal correlations to a local basis for a less error-prone read-out.

To establish an advantage for out-of-time-order experiments within these scenarios, we consider a well-known learning task, tomography of Clifford unitaries [63,64]:

*Clifford tomography.* One is given oracle access to an  $n$ -qubit Clifford unitary  $U$ . The task is to fully characterize the unitary.

In what follows, we provide an efficient protocol for Clifford tomography given oracle access to both  $U$  and  $U^\dagger$ , which involves precisely  $4n^2 + 2n$  experiments in the DQC1 model. Our protocol is a straightforward adaptation of a previous Clifford learning algorithm [64] to the DQC1 model. We also show that this protocol is robust to a finite read-out error in the measured qubit. We then summarize our hardness results, which establish that Clifford tomography with oracle access only to  $U$  requires exponentially many experiments in  $n$  in both the first and second scenarios described above. The proofs of these statements are contained in Appendixes D and E, respectively. Together with our learning protocol, these results establish an exponential advantage for out-of-time-order learning protocols in both the DQC1 model and in experiments with noisy read-out.

We begin with a few preliminaries on the Clifford group, before turning to our learning protocol. A Clifford unitary is fully characterized by its action on a generating set of Pauli operators. The simplest generating set is the set of single-qubit Pauli- $z$  and  $-x$  operators on each qubit,  $\{\sigma_z^1, \sigma_x^1, \dots, \sigma_z^n, \sigma_x^n\}$ , which contains  $2n$  total operators. A Clifford unitary maps each single-qubit Pauli operator to a Pauli string,

$$U \sigma_\alpha^i U^\dagger = (-1)^{s_\alpha^j(i) \sum_j c_{\alpha z}^{ij} c_{\alpha x}^{ij}} \prod_j (\sigma_z^j)^{c_{\alpha z}^{ij}} \prod_j (\sigma_x^j)^{c_{\alpha x}^{ij}}. \quad (4)$$

The goal of Clifford tomography is thus to determine the components of the Pauli string,  $c_{\alpha z}^{ij}$  and  $c_{\alpha x}^{ij}$ , and the sign,  $s_{\alpha}^i$ , for each input Pauli operator.

To characterize the Pauli string, we first perform a unitary operation  $V$  to map to the stabilizer of the initial state,  $\sigma_z^1$ , to the operator of interest,  $V\sigma_z^1V^\dagger = \sigma_{\alpha}^i$ . We then apply the unknown unitary  $U$ , followed by some intermediary Pauli operator  $\sigma_{\beta}^j$ , followed by the inverse unitary  $U^\dagger$ . Finally, we apply the inverse  $V^\dagger$  and measure the first qubit in the  $Z$  basis. The measurement outcome is equal to the OTOC,

$$\langle \sigma_{\beta}^j(U\sigma_{\alpha}^iU^\dagger)\sigma_{\beta}^j(U\sigma_{\alpha}^iU^\dagger) \rangle = 2c_{\alpha\beta}^{ij} - 1, \quad (5)$$

which determines the Pauli string component  $c_{\alpha\beta}^{ij}$ . Here we denote  $\bar{x} = z, \bar{z} = x$ . The OTOC takes value  $\pm 1$  because  $U\sigma_{\alpha}^iU^\dagger$  is a Pauli operator. By repeating this procedure  $4n^2$  times, we can determine the Pauli string components for each  $i, j, \alpha, \beta$ .

To characterize the signs  $s_{\alpha}^i$ , we apply the same  $V$  as before and again follow it by applying the unitary  $U$ . We then use our knowledge of the Pauli string components to apply a new unitary  $V'$  that maps the unsigned Pauli string [i.e., Eq. (4) without the sign] to  $\sigma_z^1$ . Measuring the first qubit in the  $z$  basis then gives the sign  $s_{\alpha}^i$ . Repeating this procedure  $2n$  total times gives the signs for each  $i, \alpha$ , and completes characterization of the unitary  $U$ .

Finally, we note that this protocol is trivially robust to the effect of read-out errors, since each experiment measures only a single qubit. By repeating each measurement a number  $m$  times and taking a majority vote, the effective read-out error can be reduced exponentially in  $m$ . Since the learning protocol involves  $\text{poly}(n)$  number of experiments, we can ensure with high probability that no errors occur by taking  $m = \text{polylog}(n)$ .

In Appendix D, we show that DQC1 Clifford tomography with oracle access only to  $U$  requires a number of experiments  $T$  that scales exponentially in the system size,  $T = \Omega(2^{n/2})$ . The analogous hardness result for Clifford tomography with read-out noise is contained in Appendix E, and requires a number of experiments  $T = \Omega(\frac{1}{\delta}(\frac{1}{1-\delta})^{n/2})$ , which is exponential in  $n$  whenever the read-out error  $\delta$  is nonzero. Our proofs utilize the fact that the Clifford unitaries form a 2-design [65], and therefore apply to any time-ordered learning protocols that involve a single application of the unknown unitary per experiment. This contrasts with our hardness result in the previous section, where no restriction was placed on the number of unknown unitary applications. As we have seen, this restriction can be relaxed if the Clifford unitaries are promoted to Haar random unitaries. In this case, full tomography of the unitary becomes exponentially difficult but, as shown, more coarse-grained properties such as the connectivity remain efficiently estimable via OTOCs.

## IX. EXPERIMENTAL IMPLICATIONS

Our results demonstrate that access to out-of-time-order measurements can greatly improve the learning of numerous different properties of unknown quantum dynamics. As mentioned in Sec. II, a key ingredient in these applications is the ability to reverse the time evolution of an unknown Hamilto-

nian. While it may appear surprising that time evolution can be reversed without precise knowledge of the Hamiltonian, nearly all existing strategies for time-reversal succeed in exactly this way. We outline several specific strategies (all of which have been experimentally demonstrated) below. At the end, we also discuss a distinct application of our work to validating digital quantum simulations of Hamiltonian dynamics.

The simplest approach to reversing time evolution applies to a specific class of Hamiltonians: those that possess a chiral symmetry  $C$  such that  $CHC^\dagger = -H$ . If this is the case, time evolution can be easily reversed by physically conjugating time evolution with applications of the chiral symmetry operation,  $Ce^{-iHt}C^\dagger = e^{iHt}$ . Chiral symmetries are commonplace in condensed matter physics (e.g., in the study of topological insulators), and occur in many physically relevant Hamiltonians. For example, this approach was used to reverse the time evolution of the hard-core Bose-Hubbard Hamiltonian on a bipartite lattice,  $H = \sum_{ij} J_{ij}(\sigma_i^+\sigma_j^- + \text{H.c.})$ , in an analog superconducting quantum processor [28]. In this case, the chiral symmetry is equal to the product of  $Z$  operators over one of the two sublattices.

Another widely applied approach is to use frequent global rotations, i.e., ‘‘pulse engineering,’’ to reverse the sign of all interactions of a known type. For qubits, this is possible whenever the interactions are traceless, i.e., when  $J_{xx} + J_{yy} + J_{zz} = 0$  [66]. The most widespread example of this is the dipolar interaction. In this setting, time-reversed interactions have been realized with tremendous accuracy to measure OTOCs and the Loschmidt echo in NMR [29,30], as well as in other dipolar-interacting systems such as nitrogen-vacancy centers [67].

A third approach utilizes the underlying physics that give rise to the Hamiltonian. In many quantum simulators, the interactions of the system arise from a off-resonant Raman transitions with an excited state(s). The experimenter drives the transition with a strength  $\Omega$  and detuning  $\Delta$ , which produces an effective interaction  $\sim \Omega^2/\Delta$ . In this setting, the sign of the interaction can be easily reversed by changing the detuning of the transition. This approach has been used to measure OTOCs in trapped ion analog quantum simulators [26] and to reverse the sign of spin interactions mediated by a cavity mode [68].

Finally, we anticipate that learning via OTOCs will also find useful applications for benchmarking *digital* quantum simulations [69]. Suppose one performs a series of known quantum gates, for example a Trotter decomposition, with the goal of approximating time evolution under a desired Hamiltonian. If one does not have precise knowledge of the validity of the approximation, it is desirable to in some way verify that the approximated time evolution resembles that of the desired Hamiltonian. The most direct way to do so would be to *learn the Hamiltonian* corresponding to the digital approximation, and compare the learned Hamiltonian to the desired Hamiltonian [70]. This setting is a prime candidate for learning via OTOCs. Since the time evolution is implemented by a known series of quantum gates, one can easily reverse time evolution by conjugating each individual gate and performing the gates in opposite order. By comparing the OTOCs of the digital time evolution to the OTOCs of the desired Hamiltonian, our work shows that parameters of the digital time evolution can be estimated much more efficiently in certain scenarios.

### X. DISCUSSION

In this work, we have shown that out-of-time-order measurements can provide powerful advantages for learning the dynamics of quantum systems. Our results thus highlight the potential gains that can be achieved by quantum experiments if they have sufficient control and coherence to apply time-reversed dynamics. At a conceptual level, this ties in to recent progress on using time-reversed dynamics for quantum metrology [71,72] as well as rigorous Hamiltonian learning algorithms [3,73]. Extraordinary experimental progress has led to an ever-increasing number of such platforms [26,27,29,30,74–76], and we envision that learning via OTOCs might find applications across these diverse physical contexts. Specific future directions include learning long-range cross-talk in quantum processors [77], and strongly interacting problems in NMR [7].

On the theoretical front, our results follow in the footsteps of recent works in quantum learning theory [4,5,34,78,79] to provide new avenues for exponential advantages in quantum learning. Our applications pertain to genuine questions of experimental interest, providing a new bridge between the theoretical tools of quantum learning theory and problems of practical importance in experiments.

### ACKNOWLEDGMENTS

We are grateful to Ryan Babbush, Soonwon Choi, Kostyantyn Kechedzhi, Bryce Kobrin, Lev Ioffe, Vadim Smelyanskiy, and Norman Y. Yao for insightful discussions. The numerical simulations performed in this work used the dynamite Python frontend [59], which supports a matrix-free implementation of Krylov subspace methods based on the PETSc and SLEPc packages [80]. T.S. acknowledges support from the National Science Foundation Graduate Research Fellowship Program under Grant No. DGE 1752814. J.C. is supported by a Junior Fellowship from the Harvard Society of Fellows, the Black Hole Initiative, as well as in part by the Department of Energy under grant DE-SC0007870.

### APPENDIX A: DETAILS OF NUMERICAL SIMULATIONS

Here we provide further details on the numerical simulations displayed in Figs. 2, 4, 6 of the main text.

#### 1. Correlation functions

We begin by explicitly writing down the correlation functions used in Figs. 2, 4, 6. Throughout, we denote time-evolved operators as  $V(t) \equiv U(t, 0)VU(t, 0)^\dagger$ , where the time evolution unitary is  $U(t_2, t_1) = \mathcal{T}\{e^{-i\int_{t_1}^{t_2} dt H(t)}\}$  and  $H(t)$  is the time-dependent stroboscopic Floquet Hamiltonian specified in the main text (unless otherwise stated, in Fig. 10).

In the restricted access scenario considered in Figs. 2 and 10, we use the following correlation functions:

$$\begin{aligned} C_{\text{TOC}}(t) &= \langle V_p(t)V_p(0) \rangle, \\ C_{\text{TOC}}(x, t) &= \langle V_p(t)W_x(t/2)V_p(0)W_x(t/2) \rangle, \\ C_{\text{OTOC}}(x, t) &= \langle V_p(t)W_x(0)V_p(t)W_x(0) \rangle, \end{aligned} \tag{A1}$$

where  $p$  denotes the probe qubit, and  $\langle \cdot \rangle \equiv 2^{-L}\text{tr}(\cdot)$  is an infinite temperature average. Each of these correlation functions can be measured using state preparation and read-out on the probe qubit, combined with time evolution and a single local unitary operation on the larger system. (In the case of the autocorrelation function  $C_{\text{TOC}}(t)$ , no local unitary operation is needed,  $W_x = \mathbb{1}$ .)

In principle, we envision allowing  $V, W$  to run over all local operators in the system. For instance, they could run over all  $3^w \binom{N}{w}$  Pauli operators of weight  $\leq w$ , where  $w \sim O(1)$ . This is naturally achieved by randomized measurement strategies such as shadow tomography with local Clifford unitaries and  $O(3^w)$  measurements [43,44]. In practice, we must restrict  $V, W$  to a few possible values in numerical simulations. Specifically, we take  $V = W \in \{\sigma_x, \sigma_z\}$  for TOCs, and  $V = W \in \{\sigma_z\}$  for OTOCs. The OTOC is observed to be relatively insensitive to basis of  $V$  and  $W$ , hence our choice to restrict to a single operator,  $\sigma_z$  (further, we note that adding  $\sigma_x$  OTOCs could only improve the relative advantage of OTOCs compared to TOCs). More broadly, we do not expect that adding additional pairs of  $\{V, W\}$  will change the qualitative behavior of learning via TOCs and OTOCs. Specifically, we have seen that the learning advantage of OTOCs arises from their ability to detect highly nonlocal correlations in the system (i.e., large-weight components of the time-evolved operator  $V_p(t)$ , see Appendix B for more detailed phenomenological estimates). These correlations are not detectable by any time-ordered correlator involving only few-body operators; indeed, in ergodic systems we generically expect that they are not efficiently detectable by *any* time-ordered measurement.

For Figs. 4 and 6 of the main text, we utilize correlation functions between pairs of local operators:

$$\begin{aligned} C_{\text{TOC}} &= \langle V_x(t)W_{x'}(0) \rangle, \\ C_{\text{OTOC}} &= \langle V_x(t)W_{x'}(0)V_x(t)W_{x'}(0) \rangle. \end{aligned} \tag{A2}$$

We again take  $V = W \in \{\sigma_x, \sigma_z\}$  for TOCs and  $V = W \in \{\sigma_z\}$  for OTOCs. We allow  $x, x'$  to span all qubits within a distance 2 of the link—this consists of six possible values for each of  $x, x'$ , corresponding to distances 0, 1, and 2 to both the left and right of the link. In principle, we would like  $x, x'$  to run over the entire lattice; however, in practice we observe that correlation functions involving qubits distant from the link provide little information, and so can be safely neglected.

For Fig. 5 of the main text, we utilize the correlation functions:

$$\begin{aligned} C_{\text{TOC}}^\psi &= \text{tr}(V_x(t)[W_{x'}(0) \otimes |\psi\rangle\langle\psi|_{\neq x'}]), \\ C_{\text{OTOC}}^\psi &= \text{tr}(V_x(t)W_{x'}(0)V_x(t)[W_{x'}(0) \otimes |\psi\rangle\langle\psi|_{\neq x'}]). \end{aligned} \tag{A3}$$

Here,  $|\psi\rangle\langle\psi|_{\neq x'}$  denotes the projector onto the initial product state on all qubits besides  $x'$ . We utilize this expression for the correlation functions because it is most direct to measure in experiment. For example, for the time-ordered correlator, one simply measures how an observable  $V_x$  at time  $t$  depends on the choice of initial state on qubit  $x'$  in the basis of  $W$  at time 0. To do so, one can first prepare the initial state  $|+w\rangle'_x \otimes |\psi\rangle_{\neq x'}$ , where  $|+w\rangle'_x$  denotes the positive eigenstate of  $W$  on qubit  $x$ , evolve to time  $t$ , and measure  $V_x$ ; then repeat this for the negative eigenstate  $|-w\rangle'_x$ ; and take the difference

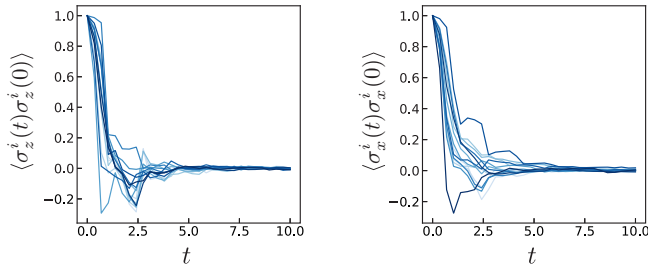


FIG. 8. The time-ordered two-point autocorrelation functions for the Hamiltonian studied in Fig. 4 of the main text, shown for all sites  $i$  in a  $L = 14$  spin chain. The decay of the autocorrelation function verifies that the Hamiltonian is in the ergodic regime and not many-body localized.

of the results. This recovers the correlation function above. In contrast, the more frequent expression for a pure state correlator, e.g.,  $\langle \psi | V_x(t) W_{x'}(0) | \psi \rangle$ , typically requires an ancilla qubit to measure. For all product states, we take  $V, W, x, x'$  identically to the infinite-temperature case above.

We now briefly comment on our numerical methods for computing the above correlation functions and the Fisher information [Figs. 2(b) and 4(b)]. We compute the infinite temperature average in the correlation functions by sampling over Haar-random initial states  $|\psi\rangle$ . To motivate this, we can insert a resolution of the identity,  $\mathbb{1} = \frac{1}{2^L} \sum_{\psi} |\psi\rangle \langle \psi|$  into the correlation functions Eq. (A2) to obtain

$$C_{\text{TOC}} = \frac{1}{2^L} \sum_{\psi} \langle \psi | V_i(t) W_j(0) | \psi \rangle, \quad (\text{A4})$$

and similarly for the OTOC. In numerics, we approximate this sum by sampling a finite number  $N_{\psi}$  of states  $|\psi\rangle$  drawn from the Haar distribution; errors in this approximation will scale as  $\sim 1/\sqrt{N_{\psi} 2^L}$ .

In Fig. 8, we plot the time-ordered correlations of the Hamiltonian considered in Fig. 4 of the main text. The correlation functions decay in time, indicating that the Hamiltonian is ergodic and not many-body localized.

In the learning problems considered in the main text [Fig. 2(a), 4(a), and 6], we take  $N_{\psi} = 25, 25, 10, 1$ , and 1 for system sizes  $L = 6, 8, 10, 12$ , and 14, respectively. In contrast, when estimating the Fisher information [Fig. 2(b) and 4(b)], we perform a large- $N_{\psi}$  extrapolation to improve precision. This is required in order to establish the asymptotic scaling of the Fisher information at large  $d$  [Fig. 2(b)] and small  $J_{\ell}$  [Fig. 4(b)]. Specifically, we compute the estimated correlation function  $C_{N_{\psi}}$  averaged over  $N_{\psi} = 1, \dots, 25$  Haar-random initial states, as well as the resultant Fisher information  $\max \text{FI}(N_{\psi}) \equiv |\partial C_{N_{\psi}} / \partial J|^2$ , maximized over all relevant correlation functions. We then perform a linear fit  $\max \text{FI}(N_{\psi}) = \max \text{FI}(\infty) + \frac{A}{N_{\psi}}$ , where  $\max \text{FI}(\infty)$  and  $A$  are fitting parameters. Finally, the fitting parameter  $\max \text{FI}(\infty)$  represents our estimation of the Fisher information at  $N_{\psi} \rightarrow \infty$ , which we plot in Figs. 2(b) and 4(b). We illustrate this procedure in Fig. 9, using the data for Fig. 2(b). On the left of Fig. 9, we plot the maximum Fisher information,  $\max \text{FI}(N_{\psi})$ , for each  $N_{\psi}$ , as a function of the distance  $d$ . We observe that in regions where  $C$  is relatively large (i.e.,

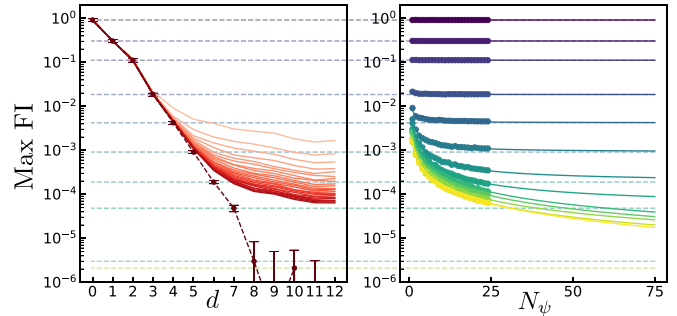


FIG. 9. Depiction of the extrapolation method used to calculate the maximum Fisher information over time-ordered correlators [Fig. 2(b)]. Each correlation function is computed for 25 Haar-random values of the state  $|\psi\rangle$  [Eq. (A4)]. For each value of  $N_{\psi}$  between 1 and 25, we choose a random subset of  $N_{\psi}$  values of  $|\psi\rangle$  and compute the average correlation function over the subset. (Left) For each value of  $N_{\psi}$ , we then compute the maximum Fisher information over all correlation functions,  $\max \text{FI}(N_{\psi})$  (solid red lines, darker lines corresponds to higher  $N_{\psi}$ ).

small  $d$ ), the estimates are quite accurate even for  $N_{\psi} = 1$ , while in regions where  $C$  is small (i.e., large  $d$ ) the Fisher information becomes successively smaller as the number of sampled states  $N_{\psi}$  increases. On the right of Fig. 9, we replot the Fisher information for each  $d$  as a function of  $N_{\psi}$ . Solid lines represent the results of the linear fit, which we observe to fit the  $N_{\psi}$  dependence of the data quite well. The extrapolated Fisher information [as displayed in Fig. 2(b)] is shown in Fig. 9 as a dashed line.

## 2. Imperfect time-reversal via cavity mode

In Fig. 6(a), we benchmark the effects of decoherence on learning by coupling the spin system to a single cavity mode. Our motivation for studying this model is twofold. First, in ergodic many-body systems the effect of local errors on OTOCs is expected to be independent of the precise microscopic form of the error [62]. We therefore expect the spin-cavity system to display similar OTOC physics to more generic local error models. Second, for  $L = 10$  spins the spin-cavity system can be exactly simulated in a Hilbert space of size  $2^L \times L$  (we assume the cavity initially has zero occupation number; since the sum of spin magnetization and the cavity occupation is conserved, the cavity occupation is upper bounded by  $L$ ). This is substantially smaller than the requirements to exactly simulate a mixed state quantum system,  $2^{2L}$ .

More specifically, the spin-cavity Hamiltonian is as follows. We modify the Floquet time evolution described in the main text to alternate between the following two Hamiltonians:

$$\begin{aligned} H_1 &= \pm H_f + g \sum_i (a^\dagger \sigma_i^- + a \sigma_i^+) + \omega a^\dagger a, \\ H_2 &= \pm H_c + g \sum_i (a^\dagger \sigma_i^- + a \sigma_i^+) + \omega a^\dagger a, \end{aligned} \quad (\text{A5})$$

where  $H_f, H_c$  are the field and coupling Hamiltonians written in the main text,  $a, a^\dagger$  are lowering/raising operators for a bosonic cavity mode,  $g = \{0.0, 0.25, 0.5\}$  is the spin-cavity

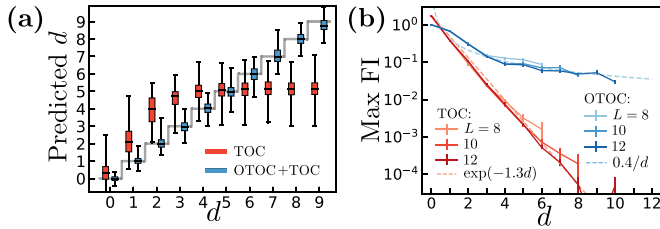


FIG. 10. Learning in the restricted access scenario under Hamiltonian evolution. Numerical simulations are performed identically to Fig. 2 but now with Hamiltonian evolution under  $(H_c + H_f)/2$  instead of Floquet evolution. In both (a) the learning task and (b) the Fisher information, the results for learning Hamiltonian dynamics are qualitatively similar to the results for learning Floquet dynamics (Fig. 2). In (b), the maximum Fisher information is averaged over 100 disorder realizations for both TOCs and OTOCs. At large  $d$ , we expect the Fisher information for Hamiltonian evolution to approach a power law decay  $\sim 1/d^4$  (see Appendix B), but this cannot be observed in our finite-size numerics.

interaction strength, and  $\omega = 1.7$  is the cavity frequency. Here, the  $\pm$  denote values during forwards/backwards time evolution; note that we do *not* reverse the spin-cavity interaction or the cavity frequency during backwards time evolution.

### 3. Learning model

We now detail the machine learning techniques used in Figs. 2(a), 4(a), and 6 of the main text, and Fig. 11(b) of the Appendix. Throughout, read-out error is mimicked by adding a random Gaussian variable with mean zero and standard deviation  $\delta$  to the exact correlation functions.

We begin with Fig. 2(a). Our goal is to predict the value of  $d$  [which specifies the geometry of the spin system, see Fig. 2(a)] from the correlation functions of the system, Eq. (A1). To do so, we train a learning model on 3000

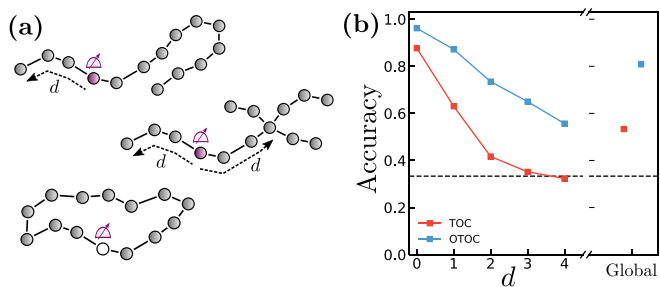


FIG. 11. (a) The three spin geometries considered in the learning task defined in the text. Each geometry consists of  $L = 14$  spins. The probe qubit (purple) is located along a subset of the system that is identical between the three geometries up to a distance  $d$  away from the probe. (b) Accuracy of classification, using correlation functions that can be measured with (left) state preparation and read-out on the probe qubit and global unitary control over the remaining system, and (right) global state preparation, unitary control, and read-out. For the former, the accuracy is plotted as a function of the distance  $d$  of the probe qubit from the geometric feature of interest. In both scenarios, access to OTOCs (blue) substantially improves the classification accuracy compare solely accessing TOCs (red).

randomly drawn disorder realizations of the Hamiltonian, consisting of 300 realizations each for  $d = 0, 1, \dots, 9$ . We test model performance on 2000 additional disorder realizations, again consisting of 200 realizations each for  $d = 0, 1, \dots, 9$ . For each disorder realization, the input to our learning model consists of the correlation functions Eq. (A1), evaluated at  $x = 2, \dots, L$  and 30 evenly spaced times between 0 and 12. We apply Gaussian distributed read-out error  $\delta = 3\%$  to each correlation function. We repeat this procedure, as well as the model training and evaluation that follows, first using only TOCs as input to the learning algorithm, and second using both TOCs and OTOCs.

Next, we input these correlation functions into a support vector regression (SVR) model with radial basis functions [81]. The radial SVR contains two hyperparameters:  $C$ , the regularization parameter, and  $\gamma$ , which controls the width of the radial basis functions. We choose  $C$  and  $\gamma$  by performing fivefold cross-validation over the sets  $C = \{10, 30, 100\}$ ,  $\gamma = \{0.03, 0.06, 0.1, 0.3, 1, 3, 6, 10\}$ . We obtain  $C = 10$ ,  $\gamma = 1$  for learning via TOCs, and  $C = 10$ ,  $\gamma = 0.03$  for learning via both TOCs and OTOCs. In the identical learning task for Hamiltonian evolution [Fig. 10(a)], we obtain  $C = 10$ ,  $\gamma = 1$  for learning via TOCs, and  $C = 100$ ,  $\gamma = 0.03$  for learning via both TOCs and OTOCs.

We now turn to Fig. 4(a) and 6. Our goal is to perform binary classification using the correlation functions Eq. (A2) to distinguish whether the link interaction strength is zero or nonzero. To do so, we simulate the correlation functions of 300 randomly drawn disorder realizations of the Hamiltonian for each link strength,  $J_\ell = \{0, 0.01, 0.017, 0.03, 0.06, 0.1, 0.17, 0.3, 0.6, 1.0\}$ . For each nonzero  $J_\ell$ , we train a learning model to perform binary classification between link strength 0 and  $J_\ell$ . We test model performance on 400 additional disorder realizations, again consisting of 200 realizations each for link strength 0 and  $J_\ell$ .

The first step of our learning model is to prune the correlation functions used as input. We do so by estimating the mutual information between each individual correlation function and the link interaction strength, and selecting the  $K$  correlation functions with the highest mutual information. Here  $K$  is a hyperparameter that will ultimately be chosen via cross-validation. To estimate the mutual information, we fit the distribution of correlation functions values over disorder realizations to a Gaussian for each link strength, and compute the Jensen-Shannon divergence between the Gaussian distributions. The Jensen-Shannon divergence is equal to the desired mutual information [82].

As before, we input the selected correlation functions into a support vector machine (SVM) with radial basis functions [81]. We now have three hyperparameters: the SVM hyperparameters  $C$  and  $\gamma$  and the number of selected correlation functions  $K$ . We choose  $C$ ,  $\gamma$ , and  $K$  by performing fivefold cross-validation over each value  $C = \{0.1, 1, 10, 100, 1000\}$ ,  $\gamma = \{0.1, 0.3, 1, 3, 10, 30\}$ . We obtain Figs. 6(b), by repeating this procedure for various simulated read-out errors,  $\delta = \{0.0001, 0.0003, 0.001, 0.003, 0.01, 0.03, 0.1\}$ . At each read-out error, we perform a linear interpolation of the classification accuracy as a function of  $J_\ell$  [as shown in Fig. 4(a) for  $\delta = 0.03$ ]. The minimum detectable link strength  $J_\ell^*$  occurs at the intersection of this interpolation with a horizontal

line (not depicted) corresponding to a classification accuracy of 90%.

Finally, we turn to Fig. 11(b) in Appendix C. In the probe qubit scenario, training and testing are performed on 300 and 200 samples respectively for each geometry and each value of  $d$ . In the global state preparation and read-out scenario, we instead use 60 and 40 samples respectively for each geometry. Our learning model consists of a support vector machine with hyperparameters chosen via fourfold cross-validation from the sets  $C = \{0.1, 1, 10\}$ ,  $\gamma = \{0.3, 3, 30\}$ . As in our previous learning tasks, we apply a read-out error  $\delta = 3\%$  to each correlation function before use in learning.

**APPENDIX B: PHENOMENOLOGICAL ESTIMATES**

In this section, we provide more detailed reasoning behind the phenomenological estimates of the Fisher information presented in the main text. We begin with the Fisher information under unitary dynamics with restricted access and then turn to the effects of imperfect time-reversal and decoherence.

**1. Fisher information in restricted access scenario**

At sufficiently large times and distances, we expect the profile of correlation functions in ergodic many-body systems to be described by only a few phenomenological parameters. For instance, in one-dimensional systems the out-of-time-order correlator is predicted to take the following functional form [41,83],

$$C_{\text{TOC}}(x, t) \approx f\left(\frac{x/v_B - t}{A\sqrt{t}}\right), \tag{B1}$$

where the phenomenological parameters  $v_B$  and  $A$  describe the butterfly velocity and the width of the OTOC wavefront, respectively. Here  $f$  is a compactly supported bump function which interpolates between zero and one and then zero again within an  $O(1)$ -sized region about the origin. Meanwhile, in systems with a local conservation law, we expect time-ordered correlators to be dominated by diffusion of the conserved quantity. This leads to the following profile for the autocorrelation function,

$$C_{\text{TOC}}(t) \sim \frac{1}{\sqrt{Dt}}, \tag{B2}$$

where  $D$  is a diffusion constant. In the absence of conserved quantities, one expects time-ordered correlation functions to instead decay exponentially in time,

$$C_{\text{TOC}}(t) \sim \exp(-\gamma t), \tag{B3}$$

parameterized by a decay rate  $\gamma$ .

To obtain the Fisher information,  $\text{FI}(J|C) = |\partial C/\partial J|^2$ , we must compute the derivative of the correlation functions with respect to a local coupling strength,  $J_y$ . To do so while leveraging the above phenomenological predictions, we must first recognize that the phenomenological parameters are themselves dependent on the local coupling strengths of the system, e.g.,  $v_B \rightarrow v_B(\{J_y\})$ . We expand on this in further detail for each case below. The resultant scaling of the Fisher information in various physical regimes is summarized in Table I.

TABLE I. Fisher information estimates in the local and global restricted access scenarios, for learning an interaction a distance  $d$  from a probe qubit.

Correlation function	Probe qubit with local unitary control	Probe qubit with global unitary control
TOC without conserved quantity	$O(\exp(-d))$ , [Fig. 2(b)]	$O(\exp(-d))$ ,
TOC with conserved quantity	$O(1/d^4)$	$O(1/d^4)$
OTOC	$O(1/d)$ , [Fig. 2(b)]	$O(1/d^2)$ ,

**a. Fisher information of OTOCs**

We begin with the Fisher information of OTOCs. Our treatment is broken into two parts, corresponding to the scenarios where the experimenter has either local or global unitary control over the larger system. The former scenario is simulated numerically in Fig. 2 of the main text.

*Local unitary control.* We consider local OTOCs [Eq. (A1)] and are interested in the dependence of the OTOC on the local coupling strengths,  $\{J_y\}$ . To approach this, we will assume that OTOC takes the same functional form as in Eq. (B1),

$$C_{\text{OTOC}}(x, t) = \langle V_p(t) W_x(0) V_p(t) W_x(0) \rangle \approx f\left(\frac{x/v_B(x) - t}{A\sqrt{t}}\right), \tag{B4}$$

but now with a *position-dependent* butterfly velocity,  $v_B(x)$ . Specifically, we assume that the effective butterfly velocity at time  $t$  receives contributions from all couplings that have been visited thus far, i.e., all  $J_y$  with  $y \lesssim x$ . Since the time to traverse a single coupling is proportional to the inverse coupling strength  $1/J_y$ , we expect the time to traverse all couplings up to a distance  $x$  to be proportional to the sum  $\sum_{y=0}^x 1/J_y$ . Equating this time to the distance divided by the effective butterfly velocity  $x/v_B(x)$ , we have

$$v_B(x) \approx \left[ \frac{1}{x} \sum_{x=0}^x \frac{1}{J_x} \right]^{-1}. \tag{B5}$$

If each coupling strength is drawn independently from some disorder realization, then at large times the butterfly velocity will be close to its typical value,  $v_B = 1/J$ .

We can now compute derivatives of the correlation function with respect to a given coupling strength via the chain rule. The derivative of the butterfly velocity is

$$\partial_{J_d} v_B(x) \approx \frac{v_B(x)^2}{J_d^2 x} \cdot \delta_{d \leq x}, \tag{B6}$$

which yields the following for the OTOC:

$$\begin{aligned} \partial_{J_d} C_{\text{OTOC}}(x, t) &\approx -\frac{x}{A\sqrt{t} v_B(x)^2} \cdot f'\left(\frac{x/v_B(x) - t}{A\sqrt{t}}\right) \cdot \partial_{J_d} v_B(x) \\ &\approx -\frac{1}{A J_d^2 \sqrt{t}} \cdot \delta_{d \leq x} \cdot f'\left(\frac{x/v_B(x) - t}{A\sqrt{t}}\right). \end{aligned} \tag{B7}$$

There are two parameters of the local OTOC chosen by a potential experimentalist: the position  $x$  of the local

perturbation, and the evolution time  $t$ . We are interested in the maximum Fisher information given an optimal choice of  $x$  and  $t$ . Observing Eq. (B7), we see that the derivative  $f'$  is maximized by the choice  $x = v_B t$ , while the delta function then sets  $v_B t = d$ . Plugging these values in, we find the Fisher information

$$\max_c \text{FI}(J|C_{\text{OTOC}}) \approx \left| \frac{f'(0)}{A J_y^2 \sqrt{v_B d}} \right|^2 \sim \frac{1}{d}. \quad (\text{B8})$$

*Global unitary control.* We now turn to an alternate experimental scenario, where one has only global unitary control over the larger system. In this scenario, the natural generalization of the correlation functions Eq. (A1) is the following:

$$\begin{aligned} C_{\text{TOC}} &= \langle V_p(t) V_p(0) \rangle, \\ C_{\text{TOC}} &= \langle V_p(t) e^{i\phi \sum_x W_x(t/2)} V_p(0) e^{-i\phi \sum_x W_x(t/2)} \rangle, \\ C_{\text{OTOC}} &= \langle V_p(t) e^{i\phi \sum_x W_x(0)} V_p(t) e^{-i\phi \sum_x W_x(0)} \rangle. \end{aligned} \quad (\text{B9})$$

Here we replace the local unitary operations of Eq. (A1) with global spin rotations,  $e^{i\phi \sum_x W_x}$ , by an angle  $\phi$  (here,  $W_x$  is a local Hermitian operator on qubit  $x$ ).

We expect the behavior of the OTOC under global control to be governed by the ‘‘size’’ of time-evolved operators [29,30,53]. The size corresponds to the average of local OTOCs over all qubits in the system [84]. In one-dimensional ergodic systems, the size grows linearly  $\sim v_B t$ , which yields the following phenomenological expectation for the global OTOC [30]:

$$C_{\text{OTOC}}^{\text{glob}} = \exp(-\phi^2 v_B(t) t). \quad (\text{B10})$$

Here we have made the butterfly velocity time-dependent to capture its dependence on the local coupling strengths,

$$v_B(t) \approx \left[ \frac{1}{v_B t} \sum_{y=0}^{v_B t} \frac{1}{J_y} \right]^{-1}, \quad (\text{B11})$$

where  $v_B = \overline{1/J}$  is the typical butterfly velocity.

Taking the derivative of the OTOC via the chain rule, we have

$$\begin{aligned} \partial_{J_d} C_{\text{OTOC}}^{\text{glob}} &\approx -\phi^2 t \cdot \partial_{J_d} v_B(t) \cdot \exp(-\phi^2 v_B(t) t) \\ &= -\phi^2 t \cdot \frac{v_B(t)^2}{v_B J_d^2 t} \cdot \delta_{d \leq v_B(t) t} \cdot \exp(-\phi^2 v_B(t) t) \\ &\approx -\phi^2 \cdot \frac{v_B}{J_d^2} \cdot \delta_{d \leq v_B t} \cdot \exp(-\phi^2 v_B t). \end{aligned} \quad (\text{B12})$$

We would like to maximize the Fisher information over the parameters  $(\phi, t)$ . This entails taking the time  $t$  to be as early as allowed by the delta function,  $t \approx d/v_B$ , in order to minimize the exponential. The correlator is then maximized by choosing  $\phi$  such that  $\phi^2 v_B t \sim 1$ . This gives a Fisher information:

$$\max_c \text{FI}(J|C_{\text{OTOC}}) \approx \left| \frac{v_B e^{-1}}{J_y^2 d} \right|^2 \sim \frac{1}{d^2}, \quad (\text{B13})$$

which decays algebraically, with an additional factor of  $d$  compared to the local unitary control scenario.

Before moving on, we briefly summarize the intuition behind the two above estimates. In both cases, an  $O(1)$  perturbation in a local coupling strength produces an  $O(1)$  shift in the location of the OTOC wavefront. With local control, this shift produces an  $O(1/\sqrt{d})$  change in the OTOC, since the OTOC wavefront is spread across a width  $\sim \sqrt{d}$  by the time it reaches the coupling. With global control, this produces an  $O(1/d)$  change in the OTOC, since the global OTOC depends on the average of  $\sim d$  individual coupling strengths. Since the Fisher information involves the square of the OTOC derivative, these lead to an  $O(1/d)$  and  $O(1/d^2)$  Fisher information, respectively.

**b. Fisher information of TOCs in absence of conserved quantities**

We now turn to a simpler case, the Fisher information of time-ordered correlators in the absence of conserved quantities [Fig. 2(b)]. Under ergodic dynamics, we expect such correlation functions to decay exponentially in time at sufficiently large times, see Eq. (B3). Now, consider the derivative of the correlation function with respect to a local coupling strength at a distance  $d$  away from the probe qubit. By causality, this derivative can only be nonzero after a time  $t \gtrsim d/v_B$ . However, at such times, the magnitude of the correlation function has already decayed by a factor of  $e^{-\gamma t}$ . This suggests that the Fisher information will decay exponentially in the distance  $d$ ,

$$\max_c \text{FI}(J|C_{\text{TOC}}) \lesssim \exp(-2\gamma x/v_B), \quad (\text{B14})$$

as observed numerically in Fig. 2(b).

**c. Fisher information of TOCs in presence of conserved quantities**

The scaling of the Fisher information for TOCs is modified in the presence of a conserved quantities. In this case, one expects the TOC at sufficiently large times to be dominated by slow diffusive dynamics of the conserved quantity. This lies in contrast to the exponential decay expected in the absence of conserved quantities.

To study this, we begin with the autocorrelation function [first line of Eq. (A1)]. Recall that the autocorrelation function can be measured with access solely to the probe qubit, and is thus accessible in both the local and global control scenarios. Similar to the case of OTOCs, we will assume that the dependence of the correlation function on the local coupling strengths is captured by replacing the diffusion constant  $D$  with a *time-dependent* value,

$$C_{\text{TOC}}(t) = \frac{1}{\sqrt{D(t)t}}. \quad (\text{B15})$$

Following the logic of the previous section, we assume the effective diffusion constant takes the form [85]

$$D(t) \sim \left[ \frac{1}{\sqrt{D t}} \sum_{y=0}^{\sqrt{D t}} \frac{1}{J_y} \right]^{-1}, \quad (\text{B16})$$

where  $D = \overline{1/J}$  is the diffusion constant’s typical value. Differentiating with respect to the local coupling strength gives

$$\partial_{J_d} D(t) \sim \frac{D(t)^2}{J_d^2 \sqrt{D t}} \cdot \delta_{d < \sqrt{D t}}. \quad (\text{B17})$$

Computing the derivative of the autocorrelation function, we have

$$\begin{aligned} \partial_{J_d} C_{\text{TOC}}(t) &= -\frac{1}{2D(t)^{3/2}t^{1/2}} \cdot \partial_{J_d} D(t) = -\frac{D(t)^{1/2}}{2J_d^2 t \sqrt{D}} \cdot \delta_{d < \sqrt{Dt}} \\ &\approx -\frac{1}{2J_d^2 t} \cdot \delta_{d < \sqrt{Dt}}. \end{aligned} \quad (\text{B18})$$

The magnitude of the derivative is maximized by taking the minimum possible time,  $t \approx d^2/D$ , which yields a Fisher information,

$$\max_C \text{FI}(J|C_{\text{TOC}}) \approx \left| \frac{D}{2J_x^2 d^2} \right|^2 \sim \frac{1}{d^4}. \quad (\text{B19})$$

This can be understood intuitively as follows. For the autocorrelation function to be sensitive to the coupling strength  $J_d$ , the conserved quantity must have spread to at least distance  $d$ . At such a distance, the magnitude of the autocorrelation function is  $O(1/d)$ , since the conserved quantity has spread over  $\sim d$  sites. In addition, the derivative with respect to an individual coupling strength is suppressed by an additional factor  $O(1/d)$ , since the autocorrelator depends only on the average (inverse) coupling strength over  $\sim d$  sites. Combining these two factors and squaring leads to an  $O(1/d^4)$  Fisher information.

We now turn to the remaining time-ordered correlation functions in Eqs. (A1) and (B9), which require either local or global unitary control over the nonprobe qubits. We will find that such correlators provide no scaling advantage beyond the autocorrelator.

We first consider the case of local unitary control [Eq. (A1)]. Physically, these correlation functions correspond to preparing an amount of the conserved quantity (e.g., a spin polarization) at the probe qubit, letting it diffuse for a time  $t/2$ , flipping the spin polarization at a qubit  $x$ , and measuring the polarization at the probe qubit after an additional time  $t/2$ . We thus expect the TOC behave as follows:

$$\begin{aligned} C_{\text{TOC}}(x, t) &= \langle V_p(t) W_x(0) V_p(t) W_x(0) \rangle \\ &\approx q(0, t) - 2q(x, t/2) \cdot q(x, t/2), \end{aligned} \quad (\text{B20})$$

where  $q(x, t) \approx (2\pi D(t)t)^{-1/2} \exp(-x^2/(2D(t)t))$  is the propagator of the conserved quantity from position 0 to position  $x$  (or vice versa). The first term is equal to the autocorrelation function. The second term arises from the spin flip at position  $x$  and time  $t/2$ . The spin flip effectively inserts a negative polarization  $-2q(x, t/2)$  on the qubit  $x$ , which propagates back to the probe qubit with amplitude  $q(x, t/2)$ .

The derivative of the second term is as follows:

$$\begin{aligned} \partial_{J_d} [q(x, t/2)^2] &= \partial_{J_d} \left[ \frac{1}{\pi D(t)t} \exp\left(-\frac{2x^2}{D(t)t}\right) \right] \\ &\approx \partial_{J_d} \left[ \frac{-1}{\pi J_y^2 D^{1/2} t^{3/2}} \exp\left(-\frac{2x^2}{D(t)t}\right) \right. \\ &\quad \left. + \frac{2x^2}{\pi J_y^2 D^{3/2} t^{5/2}} \exp\left(-\frac{2x^2}{D(t)t}\right) \right] \cdot \delta_{d < \sqrt{Dt}}. \end{aligned} \quad (\text{B21})$$

The magnitude of the derivative is maximized at  $Dt \sim x^2$ ,  $x \sim d$ , and is of order  $O(1/d^3)$ . This is subleading compared to the autocorrelation function, of order  $O(1/d^2)$ , and thus does not affect the asymptotic scaling of the Fisher information with  $d$ .

The case of a global control [Eq. (B9)] is even simpler. A global spin rotation about the  $x$  axis by an angle  $\phi$  multiplies the conserved quantity at each site by a factor of  $\cos(\phi)$ . Here we assume that the  $x$  and  $y$  components of spin that are generated by the rotation quickly decay in time if they are not conserved by the ergodic dynamics. The resulting correlation function is then given by the autocorrelation multiplied by  $\cos(\phi)$ . Again, this provides no scaling advantage in the Fisher information.

## 2. Effect of imperfect time reversal and decoherence on Fisher information

We now incorporate imperfect time-reversal dynamics into our estimates of the Fisher information of OTOCs. Previous works have been found that a wide range of experimental errors (e.g., extrinsic decoherence, coherent errors in time-reversal) have a similar effect on OTOC measurements, as long as the relevant errors are local and the dynamics are ergodic [27,29,30,60,62].

Specifically, in one-dimensional systems, one expects that the OTOC under open-system dynamics,  $\tilde{C}_{\text{OTOC}}$ , is equal to the same OTOC under unitary dynamics,  $C_{\text{OTOC}}$ , multiplied by an overall Gaussian decay in time [62]:

$$\tilde{C}_{\text{OTOC}} \approx \exp(-a\varepsilon v_B t^2) \times C_{\text{OTOC}}. \quad (\text{B22})$$

Here  $\varepsilon$  is an effective local error rate,  $v_B$  is the butterfly velocity, and  $a$  is an order one constant. The argument of the above exponential is proportional the volume of the time-evolved operator's light cone. Intuitively, Eq. (B22) states that each error in the causal past of an operator contributes a roughly equal amount to the decay of the OTOC. We note that in finite-size systems we do not expect Eq. (B22) to precisely hold, however, corrections are expected to be suppressed by  $\sim \varepsilon/J$ , where  $J$  is the local interaction strength [62], so we neglect them here.

Substituting Eq. (B22) into our estimate for the Fisher information [Eq. (B13)] and setting  $v_B t \approx d$ , we find

$$\max_C \text{FI}(J_d|\tilde{C}_{\text{OTOC}}) \sim \frac{1}{d^2} \exp(-a\varepsilon d^2/v_B). \quad (\text{B23})$$

Meanwhile, we assume that the Fisher information with respect to TOCs is comparatively unaffected by error, and thus once again follows a linear exponential decay in  $d$ :

$$\max_C \text{FI}(J_d|\tilde{C}_{\text{TOC}}) \sim \exp(-\gamma d). \quad (\text{B24})$$

Setting the two exponentials to be equal,  $\max_C \text{FI}(J_d|\tilde{C}_{\text{OTOC}}) \sim \max_C \text{FI}(J_d|\tilde{C}_{\text{TOC}})$ , we find that the OTOC continues to provide an advantage over the TOC up to

$$d \lesssim \frac{\gamma v_B}{\varepsilon}, \quad (\text{B25})$$

as quoted in the main text.

We now apply the same analysis to our second learning regime. Let us set  $v_B \sim J$  for consistency with the main text. The Fisher information of an OTOC between operators on

either side of the link with respect to the link interaction strength is now modified to

$$\max_c \text{FI}(J_\ell | \tilde{C}_{\text{OTOC}}) \sim \frac{J_\ell^4 t^2}{J^2} \exp(-a\varepsilon J t^2), \quad Jt \lesssim L. \quad (\text{B26})$$

The maximum of the Fisher information as a function of time now occurs at

$$t^* \sim \min \left\{ \sqrt{\frac{1}{\varepsilon J}}, \frac{L}{J} \right\}, \quad (\text{B27})$$

with value

$$\max_c \text{FI}(J_\ell | \tilde{C}_{\text{OTOC}}) \sim \min \left\{ \frac{J_\ell^4}{\varepsilon J^3}, \frac{J_\ell^4 L^2}{J^4} \right\}, \quad (\text{B28})$$

which differs from the unitary OTOC for sufficiently high error rates. Again, we assume that the Fisher information of TOC is not affected by error to leading order. Taking the square root of Eq. (B28), we thus find the  $L$ -fold advantage of the OTOC is replaced by a  $\sqrt{J/\varepsilon}$ -fold advantage at error rates  $\sqrt{\varepsilon/J} \gtrsim 1/L$ , as quoted in the main text.

### APPENDIX C: ADDITIONAL NUMERICS

In this section, we provide numerical results in two additional learning scenarios. We begin by repeating the simulations leading to Fig. 2 for time-independent Hamiltonian evolution instead of Floquet evolution. We then discuss learning in the restricted access scenario with global unitary control, in contrast to local unitary control as considered in the main text).

#### 1. Learning with time-independent Hamiltonian evolution

In the main text numerical simulations, we utilized Floquet time evolution in which the spin interactions and local fields were applied in a stroboscopic fashion. Our motivations for using Floquet time evolution instead of Hamiltonian time evolution were threefold. First, Floquet dynamics are prevalent in a variety of quantum systems that one might wish to learn, e.g., in digital quantum simulators, and NMR or solid-state defect setups with optical driving. Second, the Floquet dynamics considered are moderately faster to simulate via Krylov subspace methods than Hamiltonian dynamics, since the Hamiltonian of the former contains fewer terms at a given instant in time. Third, we do not expect the behavior of learning via TOCs or OTOCs under the two dynamics to qualitatively differ at moderate times and distances (although at large distances they may, see Appendix B).

Here, we check the latter assumption by repeating the numerical analysis of Fig. 2 using time-independent Hamiltonian dynamics. As shown in Fig. 10(a), we find that the results of the learning task of Fig. 2(a) behave quite similarly for Hamiltonian and Floquet dynamics. In particular, access to OTOCs continues to enable substantially more accurate predictions for the crossing distance  $d$  for all  $d \gtrsim 3$ . In Fig. 10(b), we turn to the behavior of the Fisher information as a function of a coupling's distance from the probe qubit. Unfortunately, we are not able to discern the  $\sim 1/d^4$  scaling predicted in Appendix B in our finite-size numerics. Instead, the Fisher information behaves qualitatively similar to that of

Floquet dynamics [Fig. 2(b)]. We anticipate that at sufficiently large distances the Fisher information of Hamiltonian dynamics will indeed asymptote to the expected power law decay. However, at such distances the Fisher information will likely already be too small to be useful for most practical purposes.

#### 2. Learning under restricted access with global unitary control

We now turn to learning when one has only global unitary control over the system of interest. We consider a learning task where one wishes to classify the geometry of an unknown spin system, which we assume is drawn with equal probability from the three geometries shown in Fig. 11(a). We find that access to OTOCs provides a substantial advantage in this classification task. Notably, we find that OTOCs continue to improve learning even when one has only global state preparation, control, and read-out (i.e., even in the absence of a probe qubit).

The classification problem we consider is a close variant of those introduced in the main text. We suppose that one has access to the correlation functions of an unknown Hamiltonian whose connectivity corresponds to one of the three geometries shown in Fig. 11(a). The goal is to distinguish which geometry describes the Hamiltonian. We again approach this task by training and testing a support vector machine on samples of disorder realizations, see Sec. A 3 for details.

We consider learning in two different experimental access scenarios. First, we consider the scenario where one has state preparation and read-out from a single probe qubit, and global control over the remainder of the system. In this case, we take the probe qubit to be a distance  $d$  away from any distinguishing features of the geometry (see Fig. 11), and study the learnability as a function of  $d$ . Note that we are restricted to relatively small distances,  $d \leq 4$ , owing to the particular form of the three geometries considered. We find that access to OTOCs increases the classification accuracy between 10% and 35% for all values of  $d$  [Fig. 11(b)]. For instance, OTOCs allow classification with accuracy  $\sim 65\%$  at  $d = 3$ , at which learning via TOCs has nearly trivial accuracy.

Our second scenario is even more restrictive: we suppose that one has only global state preparation, control and read-out over the entire system. Despite being commonplace in experiments such as NMR spectroscopy [8], learning in this scenario remains quite difficult in strongly interacting systems, due to the combination of time-ordered correlators decaying quickly and local information being averaged out by global control and measurement. Indeed, in our learning task, we find that learning via TOCs features a classification accuracy of only  $\sim 55\%$ . Intuitively, we expect access to global OTOCs to improve learning, as operator spreading at late times is dependent on global geometric features of the system. In keeping with this intuition, we find that learning via both TOCs and OTOCs improves the classification accuracy to  $\sim 80\%$ .

### APPENDIX D: PROOF OF HARDNESS FOR CLIFFORD TOMOGRAPHY IN DQC1

As described in the main text, an experiment within the DQC1 model consists of [36]

- (1) the initial state  $\rho = |0\rangle\langle 0| \otimes (\mathbb{1}/2)^{\otimes n-1}$ ,

- (2) arbitrary unitary operations involving all qubits,
- (3) measurement of the first qubit in the  $z$  basis.

In the main text, we showed that out-of-time-order experiments can be used to learn an  $n$ -qubit Clifford unitary  $U$  given oracle access to  $U$  and  $U^\dagger$ , within the DQC1 computational model. Here, we show that the same task requires an exponential number of measurements in  $n$  for time-ordered DQC1 experiments that involve only a single application of the unitary  $U$ .

We will in fact prove hardness for an even simpler task: distinguishing a random  $n$ -qubit Clifford unitary from the maximally depolarizing channel. Moreover, our proof of hardness will apply even if condition (i) or (iii) of the DQC1 model is relaxed. In what follows, we will relax condition (i) to be concrete, but our results are easily generalized to relaxing condition (iii) instead. Our theorem is as follows.

*Theorem 1.* (Exponential hardness of Clifford learning with time-ordered DQC1 experiments.) Consider having oracle access to either (i) a fixed  $n$ -qubit Clifford-random unitary  $U$ , or (ii) a maximally depolarizing channel. Suppose one would like to distinguish (i) and (ii) by performing experiments that each involve only a single application of the unknown quantum process, arbitrary unitary operations, and measurement of only a single qubit in the  $z$  basis with read-out error  $\delta$ . Then any learning protocol requires at least  $\Omega(\frac{2^{n/2}}{\ln(1/\delta)})$  experiments, and so is exponentially inefficient. As stated in the theorem, our proof of hardness requires the inclusion of a nonzero read-out error  $\delta$ . The required number of experiments is exponential in the system size whenever the read-out error  $\delta$  is not *double-exponentially small* in the system size. Our proof utilizes techniques from recent hardness results for learning properties of mixed stabilizer states [5].

*Proof of theorem 1.* The most general experiment within the above description prepares an initial state  $\rho$ , applies the unknown quantum process, and then applies an arbitrary known unitary  $V$ . The experiment concludes by measuring the first qubit in the  $Z$  basis with read-out error  $\delta$ . In case (i) with a Clifford unitary  $U$ , this produces a measurement outcome  $s = \pm 1$  with probability

$$p_U(s) = \text{tr} \left( \left[ \frac{1 + s\alpha\sigma_z^1}{2} \right] VU\rho U^\dagger V^\dagger \right) = \frac{1}{2} + \frac{s\alpha}{2} \text{tr}([U^\dagger V^\dagger \sigma_z^1 VU]\rho), \quad (D1)$$

where we denote the read-out fidelity  $\alpha = 1 - \delta$ . For convenience, we represent the operator in the latter expression as  $\sigma_V(t) = U^\dagger V^\dagger \sigma_z^1 VU$ . In case (ii), one instead has the constant probability distribution  $p_D(s) = 1/2$ .

A learning protocol consists of  $T$  successive experiments. We label the initial state  $\rho_r$  and known unitary  $V_r$  of each experiment by the index  $r$ . The initial state and known unitary of an experiment  $r$  may depend on the measurement outcomes  $s_{r'}$  of earlier rounds  $r' < r$ . In case (i), the joint probability distribution of the measurement outcomes of all  $T$  experiments is given by

$$p_U(s_1, \dots, s_T) = \prod_{r=1}^T \left( \frac{1}{2} + \frac{\alpha s_r}{2} \text{tr}(\rho_r \sigma_{V_r}(t)) \right). \quad (D2)$$

In case (ii), we have instead

$$p_D(s_1, \dots, s_T) = \frac{1}{2^T}, \quad (D3)$$

the constant distribution.

To show that learning is hard, we will demonstrate that the two probability distributions are close in total variational distance. The total variational distance is defined as

$$\text{TVD}(\mathbb{E}[p_U], p_D) = \sum_s |\mathbb{E}[p_U(s)] - p_D(s)|. \quad (D4)$$

From Eq. (C8) in Ref. [5], the total variational distance upper bounds the success probability  $p$  of any learning algorithm as  $p < \frac{1}{2} + \frac{1}{2} \text{TVD}(\mathbb{E}[p_U], p_D)$ .

Following Ref. [4], the total variational distance can be rewritten as

$$\text{TVD}(\mathbb{E}[p_U], p_D) = \sum_{s \text{ s.t. } \frac{\mathbb{E}[p_U(s)]}{p_D(s)} < 1} p_D(s) \cdot \left( 1 - \frac{\mathbb{E}[p_U(s)]}{p_D(s)} \right), \quad (D5)$$

where the sum runs over bitstrings  $s$  such that the fraction  $\frac{\mathbb{E}[p_U(s)]}{p_D(s)}$  is less than one. Our strategy to upper bound the total variational distance will be to lower bound the fraction  $\frac{\mathbb{E}[p_U(s)]}{p_D(s)}$ . Applying Eq. (D2), we have

$$\begin{aligned} \frac{\mathbb{E}[p_U(s)]}{p_D(s)} &= \mathbb{E} \left[ \exp \left( \sum_r \ln(1 + \alpha s_r \text{tr}(\sigma_{V_r}(t)\rho_r)) \right) \right] \\ &\geq \exp \left( \sum_r \mathbb{E}[\ln(1 + \alpha s_r \text{tr}(\sigma_{V_r}(t)\rho_r))] \right) \\ &\geq \exp \left( -c \sum_r \mathbb{E}[|\text{tr}(\sigma_{V_r}(t)\rho_r)|] \right) \\ &\geq \exp \left( -c \sum_r \mathbb{E}[\text{tr}(\sigma_{V_r}(t)\rho_r)^2]^{1/2} \right). \end{aligned} \quad (D6)$$

In the second line, we have used Jensen's inequality,  $\mathbb{E}[\exp(X)] \geq \exp(\mathbb{E}[X])$  for a random variable  $X$ . In the third line, we have used the inequality  $\ln(1 + \alpha x) \geq -c|x|$  for  $x \in [-1, \infty)$ , for the constant  $c = \ln(\frac{1}{1-\alpha}) = \ln(1/\delta)$ . In the fourth line, we have applied Holder's inequality,  $\mathbb{E}[|X|] \leq \mathbb{E}[X^2]^{1/2}$ .

We can simplify this expression by calculating the expectation value over random Clifford unitaries. Since Clifford unitaries form a 2-design, we have

$$\begin{aligned} \mathbb{E}[\text{tr}(U^\dagger \sigma_{V_r} U \rho_r)^2] &= \frac{1}{4^n - 1} \text{tr}(\sigma_{V_r}^2) \left( \text{tr}(\rho_r^2) - \frac{1}{2^n} \text{tr}(\rho_r)^2 \right) \\ &\leq \frac{2^n}{4^n - 1} \left( 1 - \frac{1}{2^n} \right) \leq \frac{1}{2^n}. \end{aligned} \quad (D7)$$

Inserting this into the above bound and performing the constant sum,  $\sum_r 1 = T$ , we have

$$\frac{\mathbb{E}[p_U(s)]}{p_D(s)} \geq \exp \left( -\frac{cT}{2^{n/2}} \right). \quad (D8)$$

Inserting this into the total variational distance gives our final bound,

$$\text{TVD}(\mathbb{E}[p_U], p_D) \leq 1 - \exp\left(-\frac{cT}{2^{n/2}}\right) \leq \frac{cT}{2^{n/2}}. \quad (\text{D9})$$

From Eq. (C8) in Ref. [5], this upper bounds the success probability  $p$  of any learning algorithm by

$$2p - 1 \leq \frac{T}{2^{n/2}} \ln(1/\delta), \quad (\text{D10})$$

where we recall  $c = \ln(1/\delta)$ . Distinguishing a random Clifford unitary from the fully depolarizing channel with success probability  $2p - 1 = \Omega(1)$  thus requires a number of experiments  $T = \Omega\left(\frac{2^{n/2}}{\ln(1/\delta)}\right)$ . ■

### APPENDIX E: PROOF OF HARDNESS FOR CLIFFORD TOMOGRAPHY WITH READ-OUT NOISE

We now consider learning an  $n$ -qubit Clifford unitary  $U$  with full read-out capabilities, but in the presence of a finite read-out error  $\delta$  per qubit. We show that this task is exponentially hard in  $n$  for time-ordered experiments that involve only a single copy of  $U$ . As in the previous section, we will in fact prove hardness for an even simpler task: distinguishing a random  $n$ -qubit Clifford unitary from the maximally depolarizing channel. Our theorem is as follows.

*Theorem 2.* (Exponential hardness of Clifford learning for time-ordered experiments with read-out noise.) Consider having oracle access to either (i) a fixed  $n$ -qubit Clifford-random unitary  $U$ , or (ii) a maximally depolarizing channel. Suppose one would like to distinguish (i) and (ii) by performing experiments that each involve only a single application of the unknown quantum process, arbitrary unitary operations, and measurement of all qubits in the  $z$  basis with read-out error  $\delta$  per qubit. Then any learning protocol requires at least  $\Omega\left(\frac{1}{n \ln(1/\delta)} \left(\frac{1}{1-\delta}\right)^{n/2}\right)$  experiments, and so is exponentially inefficient whenever  $\delta > 0$ . Our proof proceeds similarly to the proof for DQC1 hardness of Clifford learning in the previous section.

*Proof of theorem 2.* The most general experiment within the above description prepares an initial state  $\rho$ , applies the unknown quantum process, and then applies an arbitrary known unitary  $V$ . This creates the state  $VU\rho U^\dagger V^\dagger$ . The experiment concludes by measuring all qubits in the computational basis with read-out error  $\delta$  on each qubit. This produces a measurement outcome  $\mathbf{s} \in \{-1, 1\}^n$  with probability

$$p_U(\mathbf{s}) = \text{tr}(M_s VU\rho U^\dagger V^\dagger), \quad (\text{E1})$$

where we define the measurement operator

$$M_s = \bigotimes_{i=1}^n \left[ \frac{1 + s_i \alpha \sigma_z^i}{2} \right], \quad (\text{E2})$$

and the read-out fidelity  $\alpha = 1 - \delta$ . We note that as a result of the read-out error, the outcome probability is lower bounded by

$$p_U(\mathbf{s}) \geq \left(\frac{\delta}{2}\right)^n, \quad (\text{E3})$$

which is the lowest eigenvalue of  $M_s$ .

Following the steps of the previous section, we lower bound the quantity

$$\begin{aligned} & \frac{\mathbb{E}[p_U(\mathbf{s})]}{p_D(\mathbf{s})} \\ &= \mathbb{E} \left[ \exp \left( \sum_r \ln(2^n \text{tr}(M_s V_r U \rho_r U^\dagger V_r^\dagger)) \right) \right] \\ &\geq \exp \left( \sum_r \mathbb{E}[\ln(2^n \text{tr}(M_s V_r U \rho_r U^\dagger V_r^\dagger))] \right) \\ &\geq \exp \left( -c \sum_r \mathbb{E}[|1 - 2^n \text{tr}(M_s V_r U \rho_r U^\dagger V_r^\dagger)|] \right) \\ &\geq \exp \left( -c \sum_r \mathbb{E}[(1 - 2^n \text{tr}(M_s V_r U \rho_r U^\dagger V_r^\dagger))^2]^{1/2} \right). \end{aligned} \quad (\text{E4})$$

In the second line, we apply Jensen's inequality. In the third line we apply the inequality  $\ln(y) \geq -c|y - 1|$  for  $y \in [y_m, \infty)$ , for the constant  $c = \frac{1}{1-y_m} \ln\left(\frac{1}{y_m}\right)$ . From Eq. (E3), we take  $y_m = \delta^n$  which gives  $c = \frac{n}{1-\delta^n} \ln(1/\delta)$ . In the fourth line we have applied Holder's inequality,  $\mathbb{E}[|X|] \leq \mathbb{E}[X^2]^{1/2}$ .

We can now calculate the expectation value over random Clifford unitaries. We have

$$\begin{aligned} \mathbb{E}[\dots] &= 1 - 2 + 4^n \mathbb{E}[\text{tr}(M_s V_r U \rho_r U^\dagger V_r^\dagger)^2] \\ &= -1 + \frac{4^n}{4^n - 1} \left[ \text{tr}(M_s^2) \text{tr}(\rho_r^2) + \text{tr}(M_s)^2 \text{tr}(\rho_r)^2 \right. \\ &\quad \left. - \frac{1}{2^n} \text{tr}(\rho_r)^2 \text{tr}(M_s^2) - \frac{1}{2^n} \text{tr}(\rho_r^2) \text{tr}(M_s)^2 \right]. \end{aligned} \quad (\text{E5})$$

Now, we have  $\text{tr}(M_s) = 1$ ,  $\text{tr}(\rho_r) = 1$ ,  $\text{tr}(M_s^2) = (1 + \alpha^2)^n / 2^n$ , and  $\text{tr}(\rho_r^2) \leq 1$ . The above expression thus simplifies to

$$\begin{aligned} \mathbb{E}[\dots] &= -1 + \frac{4^n}{4^n - 1} \left[ \left(\frac{1 + \alpha^2}{2}\right)^n \text{tr}(\rho_r^2) + 1 \right. \\ &\quad \left. - \frac{1}{2^n} \left(\frac{1 + \alpha^2}{2}\right)^n - \frac{1}{2^n} \text{tr}(\rho_r^2) \right] \\ &= \frac{1}{4^n - 1} + \frac{4^n}{4^n - 1} \text{tr}(\rho_r^2) \left[ \left(\frac{1 + \alpha^2}{2}\right)^n - \frac{1}{2^n} \right] \\ &\quad - \frac{2^n}{4^n - 1} \left(\frac{1 + \alpha^2}{2}\right)^n \\ &< \frac{1}{4^n - 1} + \frac{4^n}{4^n - 1} \left(\frac{1 + \alpha^2}{2}\right)^n \\ &< 3 \left(\frac{1 + \alpha^2}{2}\right)^n \\ &= 3(1 - \delta + \delta^2/2)^n \\ &\leq 3(1 - \delta)^{n/2}, \end{aligned} \quad (\text{E6})$$

where in the first inequality we drop negative terms, and the second inequality holds for all  $n \geq 1$ . Inserting this into the above bound and performing the constant sum,  $\sum_r 1 = T$ , we

have

$$\frac{\mathbb{E}[p_U(s)]}{p_D(s)} \geq \exp(-3cT(1-\delta)^{n/2}). \quad (\text{E7})$$

Inserting this into the total variational distance gives our final bound,

$$\begin{aligned} \text{TVD}(\mathbb{E}[p_U], p_D) &\leq 1 - \exp(-3cT(1-\delta)^{n/2}) \\ &\leq 3cT(1-\delta)^{n/2}. \end{aligned} \quad (\text{E8})$$

This upper bounds the success probability  $p$  of any learning algorithm by

$$2p - 1 \leq \frac{1}{1-\delta^n} nT(1-\delta)^{n/2} \ln(1/\delta), \quad (\text{E9})$$

where we recall  $c = \ln(1/\delta)$ . Distinguishing a random Clifford unitary from the fully depolarizing channel with success probability  $2p - 1 = \Omega(1)$  thus requires a number of experiments  $T = \Omega\left(\frac{1}{n \ln(1/\delta)} \left(\frac{1}{1-\delta}\right)^{n/2}\right)$ . ■

- 
- [1] M. Mohseni, A. T. Rezakhani, and D. A. Lidar, Quantum-process tomography: Resource analysis of different strategies, *Phys. Rev. A* **77**, 032322 (2008).
- [2] H.-Y. Huang, M. Broughton, J. Cotler, S. Chen, J. Li, M. Mohseni, H. Neven, R. Babbush, R. Kueng, J. Preskill, and J. R. McClean, Quantum advantage in learning from experiments, *Science* **376**, 1182 (2022).
- [3] N. Wiebe, C. Granade, C. Ferrie, and D. Cory, Quantum hamiltonian learning using imperfect quantum resources, *Phys. Rev. A* **89**, 042314 (2014).
- [4] D. Aharonov, J. Cotler, and X.-L. Qi, Quantum algorithmic measurement, [arXiv:2101.04634](https://arxiv.org/abs/2101.04634).
- [5] D. Aharonov, J. Cotler, and X.-L. Qi, Quantum algorithmic measurement, *Nat. Commun.* **13**, 887 (2022).
- [6] H. Zhou, J. Choi, S. Choi, R. Landig, A. M. Douglas, J. Isoya, F. Jelezko, S. Onoda, H. Sumiya, P. Cappellaro, H. S. Knowles, H. Park, and M. D. Lukin, Quantum metrology with strongly interacting spin systems, *Phys. Rev. X* **10**, 031003 (2020).
- [7] T. E. O'Brien, L. B. Ioffe, Y. Su, D. Fushman, H. Neven, R. Babbush, and V. Smelyanskiy, Quantum computation of molecular structure using data from challenging-to-classically simulate nuclear magnetic resonance experiments, *PRX Quantum* **3**, 030345 (2022).
- [8] B. Reif, S. E. Ashbrook, L. Emsley, and M. Hong, Solid-state nmr spectroscopy, *Nat. Rev. Methods Primers* **1**, 2 (2021).
- [9] S.-T. Wang, D.-L. Deng, and L.-M. Duan, Hamiltonian tomography for quantum many-body systems with arbitrary couplings, *New J. Phys.* **17**, 093017 (2015).
- [10] N. Ezzell, B. Pokharel, L. Tewala, G. Quiroz, and D. A. Lidar, Dynamical decoupling for superconducting qubits: A performance survey, [arXiv:2207.03670](https://arxiv.org/abs/2207.03670).
- [11] E. Bairey, I. Arad, and N. H. Lindner, Learning a local hamiltonian from local measurements, *Phys. Rev. Lett.* **122**, 020504 (2019).
- [12] J. Haah, R. Kothari, and E. Tang, Optimal learning of quantum hamiltonians from high-temperature gibbs states, [arXiv:2108.04842](https://arxiv.org/abs/2108.04842).
- [13] A. I. Larkin and Y. N. Ovchinnikov, Quasiclassical method in the theory of superconductivity, *Sov. Phys. JETP* **28**, 1200 (1969).
- [14] J. Baum, M. Munowitz, A. N. Garroway, and A. Pines, Multiple-quantum dynamics in solid state nmr, *J. Chem. Phys.* **83**, 2015 (1985).
- [15] S. H. Shenker and D. Stanford, Black holes and the butterfly effect, *J. High Energy Phys.* **03** (2014) 067.
- [16] D. Stanford, Many-body chaos at weak coupling, *J. High Energy Phys.* **10** (2016) 009.
- [17] J. Maldacena, S. H. Shenker, and D. Stanford, A bound on chaos, *J. High Energy Phys.* **08** (2016) 106.
- [18] J. Maldacena and D. Stanford, Remarks on the Sachdev-Ye-Kitaev model, *Phys. Rev. D* **94**, 106002 (2016).
- [19] P. Hosur, X.-L. Qi, D. A. Roberts, and B. Yoshida, Chaos in quantum channels, *J. High Energy Phys.* **02** (2016) 004.
- [20] N. Yunger Halpern, Jarzynski-like equality for the out-of-time-ordered correlator, *Phys. Rev. A* **95**, 012120 (2017).
- [21] J. Cotler, N. Hunter-Jones, J. Liu, and B. Yoshida, Chaos, complexity, and random matrices, *J. High Energy Phys.* **11** (2017) 048.
- [22] J. S. Cotler, D. Ding, and G. R. Penington, Out-of-time-order operators and the butterfly effect, *Ann. Phys.* **396**, 318 (2018).
- [23] A. Nahum, S. Vijay, and J. Haah, Operator spreading in random unitary circuits, *Phys. Rev. X* **8**, 021014 (2018).
- [24] C. W. von Keyserlingk, T. Rakovszky, F. Pollmann, and S. L. Sondhi, Operator hydrodynamics, otocs, and entanglement growth in systems without conservation laws, *Phys. Rev. X* **8**, 021013 (2018).
- [25] S. Xu and B. Swingle, Scrambling dynamics and out-of-time ordered correlators in quantum many-body systems: A tutorial, [arXiv:2202.07060](https://arxiv.org/abs/2202.07060).
- [26] M. Gärtner, J. G. Bohnet, A. Safavi-Naini, M. L. Wall, J. J. Bollinger, and A. M. Rey, Measuring out-of-time-order correlations and multiple quantum spectra in a trapped-ion quantum magnet, *Nat. Phys.* **13**, 781 (2017).
- [27] X. Mi, P. Roushan, C. Quintana, S. Mandra, J. Marshall, C. Neill, F. Arute, K. Arya, J. Atalaya, R. Babbush *et al.*, Information scrambling in computationally complex quantum circuits, *Science* **374**, 1479 (2021).
- [28] J. Braumüller, A. H. Karamlou, Y. Yanay, B. Kannan, D. Kim, M. Kjaergaard, A. Melville, B. M. Niedzielski, Y. Sung, A. Vepsäläinen *et al.*, Probing quantum information propagation with out-of-time-ordered correlators, *Nat. Phys.* **18**, 172 (2022).
- [29] C. M. Sánchez, A. K. Chattah, and H. M. Pastawski, Emergent decoherence induced by quantum chaos in a many-body system: A loschmidt echo observation through nmr, [arXiv:2112.00607](https://arxiv.org/abs/2112.00607) (2021).
- [30] F. D. Domínguez, M. C. Rodríguez, R. Kaiser, D. Suter, and G. A. Álvarez, Decoherence scaling transition in the dynamics of quantum information scrambling, *Phys. Rev. A* **104**, 012402 (2021).
- [31] D. Burgarth, K. Maruyama, and F. Nori, Coupling strength estimation for spin chains despite restricted access, *Phys. Rev. A* **79**, 020305(R) (2009).
- [32] I. Lovchinsky, A. O. Sushkov, E. Urbach, N. P. de Leon, S. Choi, K. De Greve, R. Evans, R. Gertner, E. Bersin, C. Müller *et*

- al.*, Nuclear magnetic resonance detection and spectroscopy of single proteins using quantum logic, *Science* **351**, 836 (2016).
- [33] A. A. Gentile, B. Flynn, S. Knauer, N. Wiebe, S. Paesani, C. E. Granade, J. G. Rarity, R. Santagati, and A. Laing, Learning models of quantum systems from experiments, *Nat. Phys.* **17**, 837 (2021).
- [34] S. Chen, J. Cotler, H.-Y. Huang, and J. Li, Exponential separations between learning with and without quantum memory, [arXiv:2111.05881](https://arxiv.org/abs/2111.05881).
- [35] J. Cotler, T. Schuster, and M. Mohseni, Information-theoretic hardness of out-of-time-order correlators, *Phys. Rev. A* **108**, 062608 (2023).
- [36] E. Knill and R. Laflamme, Power of one bit of quantum information, *Phys. Rev. Lett.* **81**, 5672 (1998).
- [37] T. Morimae, K. Fujii, and J. F. Fitzsimons, Hardness of classically simulating the one-clean-qubit model, *Phys. Rev. Lett.* **112**, 130502 (2014).
- [38] To see this explicitly, we specify to the case that  $A_k, B_l$  are Pauli operators. Consider four possible operations on the density matrix  $\rho$ : the two unitary rotations  $\rho \rightarrow \frac{1 \pm iA_k}{\sqrt{2}} \rho \frac{1 \mp iA_k}{\sqrt{2}}$  (where the signs are chosen together) and the two projections  $\rho \rightarrow \frac{1 \pm A_k}{2} \rho \frac{1 \pm A_k}{2}$ . By taking linear combinations of these four possibilities in classical post-processing, we can in effect implement the matrix multiplications  $\rho \rightarrow A_k \rho$  (and similarly  $\rho \rightarrow \rho B_l$ ). Applying the appropriate operation at each time  $t_k$  (and  $t'_l$ ) gives Eq. (1).
- [39] L. D'Alessio, Y. Kafri, A. Polkovnikov, and M. Rigol, From quantum chaos and eigenstate thermalization to statistical mechanics and thermodynamics, *Adv. Phys.* **65**, 239 (2016).
- [40] E. H. Lieb and D. W. Robinson, The finite group velocity of quantum spin systems, *Commun. Math. Phys.* **28**, 251 (1972).
- [41] I. L. Aleiner, L. Faoro, and L. B. Ioffe, Microscopic model of quantum butterfly effect: Out-of-time-order correlators and traveling combustion waves, *Ann. Phys.* **375**, 378 (2016).
- [42] S. Aaronson, Shadow tomography of quantum states, *SIAM J. Comput.* **49**, STOC18 (2019).
- [43] J. Cotler and F. Wilczek, Quantum overlapping tomography, *Phys. Rev. Lett.* **124**, 100401 (2020).
- [44] H.-Y. Huang, R. Kueng, and J. Preskill, Predicting many properties of a quantum system from very few measurements, *Nat. Phys.* **16**, 1050 (2020).
- [45] S. Kay, Fundamentals of statistical signal processing: Estimation theory, *Technometrics* **37**, 465 (1993).
- [46] We note that, for simplicity of analysis, our approach neglects a few potentially interesting aspects of parameter learning. First, when learning multiple unknown parameters simultaneously, the Fisher information generalizes to a Fisher information matrix and the optimal learning strategy might involve correlations between the values of different correlation functions. We expect that the advantages we find for OTOCs will carry over to multi-parameter learning. However, we do not analyze this explicitly, in part because the matrix form makes it harder to compute phenomenological predictions to benchmark our results. Second, the Fisher information neglects aspects of parameter learning associated with local minima or barren plateaus in the learning landscape. Investigating whether access to OTOCs can improve learning when these features are important is an interesting direction for future work.
- [47] J. M. Boss, K. Chang, J. Armijo, K. Cujia, T. Rosskopf, J. R. Maze, and C. L. Degen, One- and two-dimensional nuclear magnetic resonance spectroscopy with a diamond quantum sensor, *Phys. Rev. Lett.* **116**, 197601 (2016).
- [48] E. J. Davis, B. Ye, F. Machado, S. A. Meynell, W. Wu, T. Mittiga, W. Schenken, M. Joos, B. Kobrin, Y. Lyu *et al.*, Probing many-body dynamics in a two-dimensional dipolar spin ensemble, *Nat. Phys.* **19**, 836 (2023).
- [49] T. Theis, G. X. Ortiz Jr, A. W. J. Logan, K. E. Claytor, Y. Feng, W. P. Huhn, V. Blum, S. J. Malcolmson, E. Y. Chekmenev, Q. Wang *et al.*, Direct and cost-efficient hyperpolarization of long-lived nuclear spin states on universal 15n2-diazirine molecular tags, *Sci. Adv.* **2**, e1501438 (2016).
- [50] J. W. Blanchard, D. Budker, and A. Trabesinger, Lower than low: Perspectives on zero-to ultralow-field nuclear magnetic resonance, *J. Magn. Reson.* **323**, 106886 (2021).
- [51] D. Burgarth and A. Ajoy, Evolution-free hamiltonian parameter estimation through zeeman markers, *Phys. Rev. Lett.* **119**, 030402 (2017).
- [52] K. X. Wei, C. Ramanathan, and P. Cappellaro, Exploring localization in nuclear spin chains, *Phys. Rev. Lett.* **120**, 070501 (2018).
- [53] C. M. Sánchez, A. K. Chattah, K. X. Wei, L. Buljubasich, P. Cappellaro, and H. M. Pastawski, Emergent perturbation independent decay of the loschmidt echo in a many-spin system studied through scaled dipolar dynamics, *Phys. Rev. Lett.* **124**, 030601 (2020).
- [54] D. Burgarth and K. Maruyama, Indirect hamiltonian identification through a small gateway, *New J. Phys.* **11**, 103019 (2009).
- [55] C. Di Franco, M. Paternostro, and M. S. Kim, Hamiltonian tomography in an access-limited setting without state initialization, *Phys. Rev. Lett.* **102**, 187203 (2009).
- [56] J. Zhang and M. Sarovar, Quantum hamiltonian identification from measurement time traces, *Phys. Rev. Lett.* **113**, 080401 (2014).
- [57] A. Sone and P. Cappellaro, Hamiltonian identifiability assisted by a single-probe measurement, *Phys. Rev. A* **95**, 022335 (2017).
- [58] To be precise, our numerical simulations are relevant to the scenario where the experimenter can perform  $O(1)$  local spin rotations within the time-scale set by the inverse spin interaction strength. If substantially faster local rotations are possible, then the Hamiltonian interactions could be individually tuned via local dynamical decoupling, which would allow substantially faster learning [9].
- [59] For more information visit: <https://dynamite.readthedocs.io/en/latest/>.
- [60] B. Swingle and N. Yunger Halpern, Resilience of scrambling measurements, *Phys. Rev. A* **97**, 062113 (2018).
- [61] J. R. Gonzalez Alonso, N. Yunger Halpern, and J. Dressel, Out-of-time-ordered-correlator quasiprobabilities robustly witness scrambling, *Phys. Rev. Lett.* **122**, 040404 (2019).
- [62] T. Schuster and N. Y. Yao, Operator growth in open quantum systems, *Phys. Rev. Lett.* **131**, 160402 (2023).
- [63] D. Gottesman, Identifying stabilizer states, (2008), pIRSA:08080052 see, <https://pirsa.org>.
- [64] R. A. Low, Learning and testing algorithms for the clifford group, *Phys. Rev. A* **80**, 052314 (2009).
- [65] C. Dankert, R. Cleve, J. Emerson, and E. Livine, Exact and approximate unitary 2-designs and their

- application to fidelity estimation, *Phys. Rev. A* **80**, 012304 (2009).
- [66] S. Choi, N. Y. Yao, and M. D. Lukin, Dynamical engineering of interactions in qudit ensembles, *Phys. Rev. Lett.* **119**, 183603 (2017).
- [67] C. Zu, F. Machado, B. Ye, S. Choi, B. Kobrin, T. Mittiga, S. Hsieh, P. Bhattacharyya, M. Markham, D. Twitchen *et al.*, Emergent hydrodynamics in a strongly interacting dipolar spin ensemble, *Nature (London)* **597**, 45 (2021).
- [68] E. J. Davis, G. Bentsen, L. Homeier, T. Li, and M. H. Schleier-Smith, Photon-mediated spin-exchange dynamics of spin-1 atoms, *Phys. Rev. Lett.* **122**, 010405 (2019).
- [69] A. J. Daley, I. Bloch, C. Kokail, S. Flannigan, N. Pearson, M. Troyer, and P. Zoller, Practical quantum advantage in quantum simulation, *Nature (London)* **607**, 667 (2022).
- [70] J. Carrasco, A. Elben, C. Kokail, B. Kraus, and P. Zoller, Theoretical and experimental perspectives of quantum verification, *PRX Quantum* **2**, 010102 (2021).
- [71] E. Davis, G. Bentsen, and M. Schleier-Smith, Approaching the heisenberg limit without single-particle detection, *Phys. Rev. Lett.* **116**, 053601 (2016).
- [72] Z. Li, S. Colombo, C. Shu, G. Velez, S. Pilatowsky-Cameo, R. Schmied, S. Choi, M. Lukin, E. Pedrozo-Peñafiel, and V. Vuletić, Improving metrology with quantum scrambling, *Science* **380**, 1381 (2023).
- [73] A. Dutkiewicz, T. E. O'Brien, and T. Schuster, The advantage of quantum control in many-body hamiltonian learning, [arXiv:2304.07172](https://arxiv.org/abs/2304.07172).
- [74] J. Li, R. Fan, H. Wang, B. Ye, B. Zeng, H. Zhai, X. Peng, and J. Du, Measuring out-of-time-order correlators on a nuclear magnetic resonance quantum simulator, *Phys. Rev. X* **7**, 031011 (2017).
- [75] K. A. Landsman, C. Figgatt, T. Schuster, N. M. Linke, B. Yoshida, N. Y. Yao, and C. Monroe, Verified quantum information scrambling, *Nature (London)* **567**, 61 (2019).
- [76] M. S. Blok, V. V. Ramasesh, T. Schuster, K. O'Brien, J. M. Kreikebaum, D. Dahlen, A. Morvan, B. Yoshida, N. Y. Yao, and I. Siddiqi, Quantum information scrambling in a superconducting qutrit processor, *Phys. Rev. X* **11**, 021010 (2021).
- [77] M. Sarovar, T. Proctor, K. Rudinger, K. Young, E. Nielsen, and R. Blume-Kohout, Detecting crosstalk errors in quantum information processors, *Quantum* **4**, 321 (2020).
- [78] S. Chen, J. Cotler, H.-Y. Huang, and J. Li, A hierarchy for replica quantum advantage, [arXiv:2111.05874](https://arxiv.org/abs/2111.05874).
- [79] J. Cotler, H.-Y. Huang, and J. R. McClean, Revisiting dequantization and quantum advantage in learning tasks, [arXiv:2112.00811](https://arxiv.org/abs/2112.00811) (2021).
- [80] V. Hernandez, J. E. Roman, and V. Vidal, SlepC: A scalable and flexible toolkit for the solution of eigenvalue problems, *ACM Trans. Math. Softw.* **31**, 351 (2005).
- [81] L. Buitinck, G. Louppe, M. Blondel, F. Pedregosa, A. Mueller, O. Grisel, V. Niculae, P. Prettenhofer, A. Gramfort, J. Grobler, R. Layton, J. VanderPlas, A. Joly, B. Holt, and G. Varoquaux, API design for machine learning software: Experiences from the scikit-learn project, [arXiv:1309.0238](https://arxiv.org/abs/1309.0238).
- [82] J. Lin, Divergence measures based on the shannon entropy, *IEEE Trans. Inf. Theory* **37**, 145 (1991).
- [83] A. Nahum, J. Ruhman, S. Vijay, and J. Haah, Quantum entanglement growth under random unitary dynamics, *Phys. Rev. X* **7**, 031016 (2017).
- [84] X.-L. Qi and A. Streicher, Quantum epidemiology: Operator growth, thermal effects, and syk, *J. High Energy Phys.* **08** (2019) 012.
- [85] S. Revathi and V. Balakrishnan, Effective diffusion constant for inhomogeneous diffusion, *J. Phys. A: Math. Gen.* **26**, 5661 (1993).